CMS Physics Analysis Summary

Contact: cms-pag-conveners-susy@cern.ch 2020/07/29

Search for physics beyond the standard model in final states with two opposite-charge same-flavor leptons, jets, and missing transverse momentum in pp collisions at 13 TeV

The CMS Collaboration

Abstract

A search for phenomena beyond the standard model (BSM) is presented in final states with two opposite-charge same-flavor leptons, jets, and missing transverse momentum. The search is performed in a data sample of pp collisions at $\sqrt{s} = 13$ TeV, collected by the CMS experiment at the LHC, and corresponding to an integrated luminosity of 137 fb^{-1}. Three potential signatures of BSM physics are explored: (i) an excess of events with a lepton pair whose invariant mass is consistent with the Z boson mass; (ii) a kinematic edge in the invariant mass distribution of the lepton pair; (iii) the non-resonant production of two leptons. The observed event yields are consistent with the predicted standard model backgrounds. The results are used to constrain models of BSM physics that result in the production of pairs of gluinos, squarks, sleptons, or charginos and neutralinos. Upper limits at 95% CL are set on the production cross-section of supersymmetric particles. Searching for (i) allows to probe gluino masses up to 1875 GeV, as well as chargino (neutralino) masses up to 750 (800) GeV; searching for (ii) allows to exclude light-flavor (bottom) squark masses up to 1800 (1600) GeV; finally, by searching for (iii) slepton masses up to 650 GeV can also be excluded.

1 Introduction

The standard model (SM) of particle physics has been proven during the last decades to successfully and accurately describes most observations in particle physics. Despite its success, the SM is not a complete theory, as it can not explain a number of experimental observations, such as the existence of dark matter [1]. Supersymmetry (SUSY) [2–9] extends the SM, with the addition of a new symmetry that relates fermions and bosons: for each fermion (boson) of the SM, SUSY predicts the existence of a boson (fermion) partner. The new supersymmetric partners of the SM particles could contribute to the stabilization of the Higgs (H) boson mass, and favor the unification of the electroweak (EW) and strong interactions [10]. Moreover, if R-parity [11] is conserved, then the lightest SUSY particle (LSP) is predicted to be stable, neutral, and possibly massive, thus representing a suitable candidate for dark matter.

This note presents a search for signatures of physics beyond the SM (BSM) in events with two opposite-charge (OC), same-flavor (SF) leptons (electrons, e, or muons, μ), referred to as OCSF leptons, and missing transverse momentum. A data set of proton-proton (pp) collisions is used, corresponding to an integrated luminosity of 137 fb^{-1}, collected with the CMS detector at the CERN LHC in 2016–2018, at a center-of-mass energy $\sqrt{s} = 13\,\text{TeV}$.

Results are interpreted by means of R-parity conserving SUSY models predicting final states with a pair of OCSF leptons. This signature occurs in a variety of SUSY scenarios where the leptons emerge either from on-shell or off-shell Z boson decays, or from the decay of the SUSY partners of the SM leptons (sleptons, $\widetilde{\ell}$). Leptons from the decay of an on-shell Z boson would produce an excess of events with a dilepton invariant mass close to the Z boson mass. Otherwise, in the case of off-shell Z boson decays, the excess would present a characteristic edge-like shape in the dilepton invariant mass spectrum.

The search is designed to cover a range of Simplified Model Spectra (SMS) [12], that are classified according to the underlying SUSY model, the production mechanism (electroweak or strong production), and to the absence, presence, or abundance of quarks in the final state. Some of these models are inspired by gauge-mediated supersymmetry breaking (GMSB) with the gravitino as the LSP. Diagrams for the electroweak production models considered are shown in Figure 1 and the strong production ones in Figure 2. Table 1 specifies the notation used in this note for the SUSY particles involved in these processes. The SMSs considered here assume that all SUSY particles other than those directly involved in the process are decoupled and too heavy to be produced directly.

Table 1: List of SUSY particles involved in the models considered, together with the symbols representing them.

Particle	Symbol
Slepton	$\widetilde{\ell}$
Lightest neutralino	$\widetilde{\chi}_1^0$
Next-to-lightest neutralino	$\widetilde{\chi}_2^0$
Lightest chargino	$\widetilde{\chi}_1^{\pm}$
Gravitino	$\widetilde{\mathrm{G}}$
Squark	$\widetilde{\mathrm{q}}$
Sbottom	$\widetilde{\mathrm{b}}$
Gluino	$\widetilde{\mathrm{g}}$

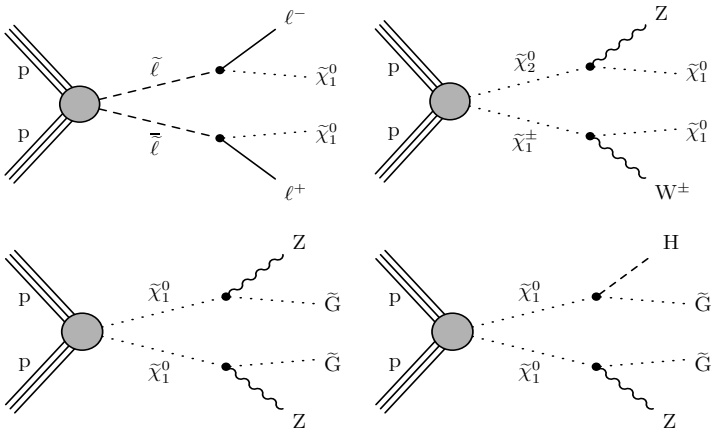

Figure 1: Diagrams for models of (upper left) direct slepton pair production, (upper right) neutralino/chargino production, and GMSB neutralino pair production with (lower left) ZZ and (lower right) ZH bosons in the final state, where in the latter model the $\tilde{\chi}_1^0$ decays to H or Z with a 50% probability for each of the modes. Such models predict the involved SUSY particles to be produced via EW interaction, with absence or moderate presence of quarks in the final state.

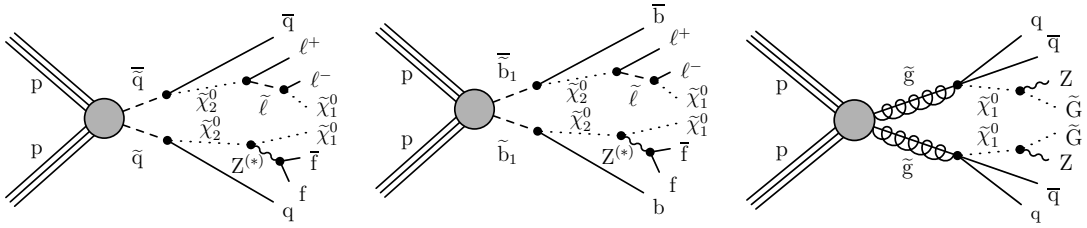

Figure 2: Diagrams for models of (left) $\tilde{q}$ and (center) $\tilde{b}$ pair production. Such models feature a mass edge from the decay of a $\tilde{\chi}_2^0$ via an intermediate slepton, $\tilde{\ell}$. In the diagram in the center, a pair of b quarks is present in the final state. In these models the $\tilde{\chi}_1^0$ mass is fixed to 100 GeV, while the mass of the slepton is taken to be equidistant from the masses of the two neutralinos. (Right) Diagram for a model of GMSB gluino pair production, where each $\tilde{g}$ decays into a pair of quarks and a neutralino. The neutralino then decays to a Z boson and an LSP. All these models assume strong production of SUSY particles and predict abundance of quarks in the final state.

Particles produced in the decay of an object produced with a large boost, as it happens in some models with large mass splitting between SUSY particles and their decay products, are expected to be emitted in a collinear configuration. As shown in the upcoming sections, this feature is accounted for in the object and event selection, in an attempt to maximize the sensitivity of the search to such signatures.

Similar searches have been performed previously by the CMS [13–20] and ATLAS [21–24] Collaborations in data at center-of-mass energies of 8 and 13 TeV. None of these searches reported any evidence for BSM physics, and results were used to constrain a range of (simplified) SUSY models.

2 The CMS detector

The central feature of the CMS apparatus is a superconducting solenoid, 13 m in length and 6 m in diameter, that provides an axial magnetic field of 3.8 T. Within the solenoid volume are various particle detection systems. Charged-particle trajectories are measured by silicon pixel and strip trackers, covering $0 < \phi < 2\pi$ in azimuth and $|\eta| < 2.5$, where the pseudorapidity η is defined as $-\ln[\tan(\theta/2)]$, with θ being the polar angle of the trajectory of the particle with respect to the counterclockwise beam direction. The pixel tracker was upgraded before the start of the data taking period in 2017, providing one additional layer of measurements compared to the older tracker. A crystal electromagnetic calorimeter (ECAL) and a brass and scintillator hadron calorimeter (HCAL) surround the tracking volume. The calorimeters provide energy and direction measurements of electrons and hadronic jets. Muons are detected in gas-ionization detectors embedded in the steel flux-return yoke outside the solenoid. The detector is nearly hermetic, allowing for momentum balance measurements in the plane transverse to the beam direction. A two-tier trigger system selects events of interest for physics analysis. The first level of the CMS trigger system, composed of custom hardware processors, uses information from the calorimeters and muon detectors to select the most interesting events in a fixed time interval of less than 4 μs. The high-level trigger processor farm further decreases the event rate from around 100 kHz to about 1 kHz, before data storage. A more detailed description of the CMS detector and trigger system, together with a definition of the coordinate system used and the relevant kinematic variables, can be found in Refs. [25, 26]. The pixel tracker upgrade is described in detail in Ref. [27].

3 Data sets, triggers, and object reconstruction

We use data samples of events with two OC leptons ($e^{\pm}e^{\mp}$, $\mu^{\pm}\mu^{\mp}$, or $e^{\pm}\mu^{\mp}$) . For signal regions (SRs), only SF leptons ($e^{\pm}e^{\mp}$ or $\mu^{\pm}\mu^{\mp}$) are selected, while $e^{\pm}\mu^{\mp}$ events are used in control regions (CRs). These events are preselected using dilepton triggers that require the magnitude of the transverse momentum (p_T) of the highest (next-to-highest) p_T lepton to be larger than a threshold ranging from 17 to 23 (8 to 12) GeV, depending on the data taking period and the lepton flavor. These triggers additionally require the leptons to pass isolation criteria. In order to retain high efficiency for boosted topologies that yield nearly collinear lepton pairs, we also use a second set of triggers with higher p_T thresholds of 25 to 37 (8 or 33) GeV but without any isolation requirement. Trigger efficiencies are measured in events selected using triggers based on the magnitude of the transverse momentum imbalance in the event, $\vec{p}_T^{\,miss}$, which is denoted as p_T^{miss}, and are found to be 85–95%. Additionally, a γ+jets sample is collected with a set of photon triggers, with p_T thresholds ranging between 50 and 200 GeV. A subset of these triggers, with lower p_T thresholds, are prescaled to keep the trigger rate under control. Events collected with prescaled triggers are reweighted accordingly.

The particle-flow (PF) algorithm [28] aims at reconstructing and identifying each particle in an event by combining the information from all elements of the CMS detector. The particles reconstructed with this algorithm are referred to as PF candidates. Collision events are selected requiring at least one reconstructed vertex. Due to the presence of additional pp interactions within the same or nearby bunch crossings (pileup), the candidate vertex with the largest value of summed physics-object p_T^2 is taken to be the primary pp interaction vertex (PV). The physics objects are the jets, clustered using the jet finding algorithm [29, 30] with the tracks assigned to candidate vertices as inputs, and the associated missing transverse momentum, taken as the negative vector sum of the p_T of those jets.

Muons and electrons are identified among the PF candidates by exploiting specific signatures in the CMS subdetectors [31, 32]. Leptons reconstructed in the transition region between the barrel and endcap of the ECAL ($1.4 < |\eta| < 1.6$) are rejected to avoid efficiency differences between electrons and muons. For both lepton flavors, the impact parameter with respect to the PV is required to be less than 0.5 mm in the transverse plane and less than 1 mm along the beam direction. In order to reject lepton candidates in hadronic jets, leptons are required to be isolated from other particles in the event. The lepton isolation variable is defined as the scalar sum p_T of all objects in a cone around the lepton. The cone size, defined as $\Delta R = \sqrt{(\Delta\phi)^2 + (\Delta\eta)^2}$, varies as a function of the lepton p_T: $\Delta R = 0.2$ if $p_T < 50\,\text{GeV}$, $\Delta R = 10\,\text{GeV}/p_T$ for $50 < p_T < 200\,\text{GeV}$, and $\Delta R = 0.05$ otherwise. This choice prevents efficiency losses due to overlap of leptons and jets in events with high jet multiplicity. Degradation of the performance due to pileup is mitigated by selecting only charged particles that originate from the lepton production vertex in the calculation of the isolation variable. Additionally, residual contributions from pileup to the neutral component of the isolation are subtracted in an average way, as described in Ref. [32]. The isolation variable is required to be smaller than 10 (20)% of the electron (muon) p_T. The electron and muon selections have been optimized to maximize the corresponding efficiency, as well as to retain the same selection efficiency for the two flavors.

Photons are required to pass identification criteria based on the cluster shape in the ECAL and on the fraction of their energy deposited in the HCAL [33]. Photons must have $p_T > 50\,\text{GeV}$, and be within $|\eta| < 2.4$, excluding the "transition region" of $1.4 < |\eta| < 1.6$ between the ECAL barrel and endcap. Photons are required to be isolated from other PF candidates within a cone of $\Delta R = 0.3$. To distinguish photons from electrons, we reject photons that can be connected to a pattern of hits in the pixel detector, indicating the presence of a charged particle track. To remove the contamination from events with significant p_T^{miss} due to mismeasurements of the photon energy, events with $\Delta\phi(\vec{p}_T^{\,\gamma}, \vec{p}_T^{\,\text{miss}}) < 0.4$ are rejected. The missing transverse momentum $\vec{p}_T^{\,\text{miss}}$ is defined as the negative vector p_T sum of all the PF candidates in the event, and, as already stated, its magnitude is referred to as p_T^{miss}.

To further suppress additional leptons in the final state, isolated charged-particle tracks identified as PF candidates are considered. Particle-flow candidates identified as leptons (charged hadrons) are required to have $p_T > 5\,(10)\,\text{GeV}$.

Jets are clustered from PF candidates, excluding charged hadrons not associated with the PV, using the anti-k_T clustering algorithm [29] with a distance parameter of 0.4, implemented in the FastJet package [30, 34], unless specified otherwise. Jets are required to satisfy $|\eta| < 2.4$ and $p_T > 35\,\text{GeV}$, where the p_T is corrected for nonuniform detector response and pileup effects [35, 36]. Corrections to the jet energy are propagated to $\vec{p}_T^{\,\text{miss}}$ using the procedure developed in Ref. [35]. As isolated prompt leptons or photons may be included in the jet definition, jets are removed from the event if they point within $\Delta R < 0.4$ of any of the selected leptons or the highest p_T photon. A deep neural network-based algorithm [37] is used to identify jets produced by the hadronization of b quarks, using a working point that yields an identification efficiency of about 70% and misidentification probabilities of 1% and 12% for light-flavor or gluon jets and charm jets, respectively. We count b-tagged jets with $|\eta| < 2.4$ and $p_T > 25$ or 35 GeV, depending on the SR, as described in Section 4.

Jets built using the anti-k_T clustering algorithm with a distance parameter of 0.8 are used to identify hadronically-decaying, high-momentum, $W^{\pm}$ and Z bosons, since their decay products are collimated into a single large radius jet. The $W^{\pm}/Z$ boson candidates are required to have $p_T > 200\,\text{GeV}$ and soft-drop mass between 65 and 105 GeV. The soft-drop mass is a groomed jet mass calculated using the mass drop algorithm [38] with angular exponent $\beta = 0$

and soft cutoff threshold $z_{cut} < 0.1$. Additional selection criteria are imposed on the ratio between the 2-subjettiness and 1-subjettiness variable [39], $\tau_{21} = \tau_2/\tau_1$, to select jets compatible with the 2-prong structure expected in $W^{\pm}$ and Z boson decays [40].

Samples of simulated events are used to model signal and background processes. The generation of BSM signal samples is performed using the MADGRAPH5_aMC@NLO program at leading order (LO) precision, with up to two additional partons in the matrix element calculation. Samples of Drell–Yan (DY) processes and photons produced in association with jets (γ+jets) are generated with the MADGRAPH5_aMC@NLO 2.3.3 event generator [41] at LO precision, with up to four additional partons in the matrix element calculations. Standard model $t\bar{t}V$ and VVV ($V = W^{\pm}, Z$) events are produced with the same generator at next-to-leading order (NLO) precision. Other SM processes, such as WW, $q\bar{q} \to ZZ$, $t\bar{t}$, and single top quark production, are generated at NLO precision using POWHEG (v1.0, or v2.0) [42–44]. A generator-level p_T-dependent next-to-NLO (NNLO)/NLO κ-factor [45–47], ranging from 1.1 to 1.3, is applied to Monte Carlo $q\bar{q} \to ZZ$ events in order to account for the missing higher order matrix element calculations. Finally, the $gg \to ZZ$ process is generated at LO using MCFM 7.0 [48–50] and is normalized to the NLO cross section calculations [51].

In all cases, generators are interfaced with PYTHIA 8.2 [52] for the modeling of fragmentation and parton showering. For samples generated at LO (NLO) precision, the MLM [53] (FxFx [54]) prescription is used to match partons from the matrix element calculation to those from the parton showers. The CUETP8M1 [55] PYTHIA 8.2 tune is used for the 2016 SM background and signal samples. For 2017 and 2018, the CP5 and CP2 tunes [56] are used for the SM background and signal samples, respectively. The NNPDF3.0LO (NNPDF3.0NLO) [57] parton distribution functions (PDFs) are used to generate the 2016 LO (NLO) samples, while the NNPDF3.1LO (NNPDF3.1NNLO) [58] PDFs are used for the 2017 and 2018 samples.

For all SM processes, the detector response is simulated with a GEANT4 model [59] of the CMS detector, while BSM samples are processed using the CMS fast simulation framework [60, 61]. The simulation programs account for the different detector conditions in the three years of data taking. Multiple pp interactions are superimposed on the hard collision, and the simulated samples are reweighted in such a way that the number of collisions per bunch crossing accurately reflects the distribution observed in data.

Cross sections at NLO and NNLO [41, 44, 62–65] are used to normalize the simulated background samples, while signal cross sections are calculated at NLO plus next-to-leading-logarithmic (NLL) order in α_S [66–73] for the EW sector, or at approximately NNLO plus next-to-NLL (NNLL) order in α_S [74–85] for the strong sector. The production cross sections for the EW GMSB scenario (see Section 1) are computed in a limit of mass-degenerate higgsino states $\tilde{\chi}_1^{\pm}$,$\tilde{\chi}_2^0$, and $\tilde{\chi}_1^0$, with all the other SUSY particles assumed to be heavy and decoupled.

4 Event selection

The SRs are designed to be sensitive to a range of BSM physics models, while maintaning the SM background under control. Four main event samples are defined starting from a baseline selection, and are defined to maximize the sensitivity to specific BSM processes. Since the statistical interpretation of the results is performed separately in each sample, some of the samples are non disjoint. The first (second) sample targets strong (EW) BSM processes with an on-shell Z boson in the decay chain. Another sample, referred to as "edge" sample, targets strong BSM production with an off-shell Z boson or a slepton in the decay chain. Finally, the requirements for the fourth sample are designed to be sensitive to the the direct production of a slepton pair.

The selections used to define all samples are summarized in Table 2. In addition to the SRs, we also define a set of CRs to be used in the estimation of the main SM backgrounds.

The baseline selection requires the presence of two OC leptons with $p_{\mathrm{T}} > 25\,(20)$ GeV for the highest (next-to-highest) p_{T} lepton, and $|\eta| < 2.4$ for both leptons. In each event, lepton flavors must be consistent with the corresponding requirement at trigger level, e.g., if an event is preselected using a $\mathrm{e}^{\pm}\mathrm{e}^{\mp}$ trigger, both leptons are required to be electrons. To avoid differences in reconstruction and isolation efficiencies between electrons and muons in boosted topologies, the two highest p_{T} leptons are required to be separated by a distance $\Delta R > 0.1$. The invariant mass $m_{\ell\ell}$ of the dilepton system and its transverse momentum $p_{\mathrm{T}}^{\ell\ell}$ are required to be larger than 20 and 50 GeV, respectively. In the SRs, the two highest p_{T} leptons are also required to have the same flavor, $\mathrm{e}^{\pm}\mathrm{e}^{\mp}$ or $\mu^{\pm}\mu^{\mp}$, while for a number of CRs the presence of different flavor (DF) leptons, $\mathrm{e}^{\pm}\mu^{\mp}$, is required.

In order to suppress backgrounds where instrumental $p_{\mathrm{T}}^{\mathrm{miss}}$ arises from jet energy mismeasurements, the two highest p_{T} jets in the event are required to have a separation in ϕ from $\vec{p}_{\mathrm{T}}^{\,\mathrm{miss}}$ of at least 0.4 ($\Delta\phi(\vec{p}_{\mathrm{T}}^{\,\mathrm{j}_{1,2}}, \vec{p}_{\mathrm{T}}^{\,\mathrm{miss}}) \geq 0.4$). In regions with only one jet, this criterion is only applied to the single jet. If the aforementioned jet is a $\mathrm{W}^{\pm}/\mathrm{Z}$ candidate, the selection is tightened to $\Delta\phi > 0.8$.

4.1 The on-Z search regions

Events with a Z boson candidate define the so-called on-Z SRs. In such events, the dilepton invariant mass is required to be $86 < m_{\ell\ell} < 96$ GeV. Events containing additional leptons or charged isolated tracks, as described in Section 3, are rejected.

4.1.1 Strong on-Z search regions

Six disjoint event categories are defined that are expected to be sensitive to strong production of SUSY particles. These categories are defined based on the number of jets and the presence of b-tagged jets. Further requirements are made on the M_{T2} variable defined below, as well as H_{T}, the scalar sum of jet p_{T}. Each category is further divided in multiple bins of $p_{\mathrm{T}}^{\mathrm{miss}}$, as indicated in Table 2.

The M_{T2} variable [86, 87] is used to reduce the $\mathrm{t\bar{t}}$ background contribution. It is constructed starting from $\vec{p}_{\mathrm{T}}^{\,\mathrm{miss}}$ and two visible objects, as:

$$M_{\mathrm{T2}} = \min_{\vec{p}_{\mathrm{T}}^{\,\mathrm{miss}\,(1)} + \vec{p}_{\mathrm{T}}^{\,\mathrm{miss}\,(2)} = \vec{p}_{\mathrm{T}}^{\,\mathrm{miss}}} \left[\max\left(M_{\mathrm{T}}^{(1)}, M_{\mathrm{T}}^{(2)} \right) \right], \tag{1}$$

where $\vec{p}_{\mathrm{T}}^{\,\mathrm{miss}\,(i)}$ ($i = 1, 2$) are trial vectors obtained by decomposing $\vec{p}_{\mathrm{T}}^{\,\mathrm{miss}}$, and $M_{\mathrm{T}}^{(i)}$ is the transverse mass obtained by pairing $\vec{p}_{\mathrm{T}}^{\,\mathrm{miss}\,(i)}$ with either of the two visible objects. When evaluated using the two selected leptons as the visible objects, the resulting quantity is referred to as $M_{\mathrm{T2}}(\ell\ell)$, and exhibits an endpoint at the $\mathrm{W}^{\pm}$ boson mass in $\mathrm{t\bar{t}}$ events. A requirement of $M_{\mathrm{T2}}(\ell\ell) > 80\,(100)$ GeV is therefore applied in the b veto (b tag) regions in order to suppress such background contribution.

4.1.2 Electroweak on-Z search regions

The first EW on-Z event category (referred to as "VZ" category) targets final states with a diboson pair (ZZ or $\mathrm{ZW}^{\pm}$), with a leptonically decaying Z and with the second boson decaying hadronically. Depending on its momentum, the decay products of the hadronically decaying

boson can either be collimated or well separated into two jets. For this reason we define two subcategories, "boosted" and "resolved", subdivided into several bins of $p_{\mathrm{T}}^{\mathrm{miss}}$.

For the resolved subcategory we require the presence of at least two jets. Furthermore, the invariant mass of the two jets that are closest in ϕ, m_{jj}, is required to be less than 110 GeV, to be consistent with the hadronic decay of a $\mathrm{W}^{\pm}$ or Z boson. To reduce $\mathrm{t\bar{t}}$ background, we reject events with b-tagged jets with $p_{\mathrm{T}} > 25$ GeV or with $M_{\mathrm{T2}}(\ell\ell) < 80$ GeV.

In the boosted subcategory we require the presence of a large radius jet with $p_{\mathrm{T}} > 200$ GeV, consistent with a hadronically decaying $\mathrm{W}^{\pm}/\mathrm{Z}$ boson candidate ($n_{\mathrm{W}^{\pm}/\mathrm{Z}}^{\mathrm{boosted}} \geq 1$). In order to ensure that the boosted and resolved categories are disjoint, events with $n_{\mathrm{j}} \geq 2$ are not accepted in the boosted region.

Another EW on-Z category, referred to as "HZ" category, is designed to be sensitive to events with a $\mathrm{H} \to \mathrm{b\bar{b}}$ decay. Events belonging to this category must have exactly two b-tagged jets with $p_{\mathrm{T}} > 25$ GeV and an invariant mass $m_{\mathrm{bb}} < 150$ GeV. To reduce the $\mathrm{t\bar{t}}$ background contribution, the M_{T2} variable is calculated using combinations consisting of one lepton and one b-tagged jet as visible objects. Each lepton is paired with a b-tagged jet, and M_{T2} is evaluated for all possible combinations. The smallest value of M_{T2} is denoted by $M_{\mathrm{T2}}(\ell\mathrm{b}\ell\mathrm{b})$. We require $M_{\mathrm{T2}}(\ell\mathrm{b}\ell\mathrm{b}) < 200$ GeV, since this variable in $\mathrm{t\bar{t}}$ events has an endpoint at the top mass. The events are finally subdivided in bins of $p_{\mathrm{T}}^{\mathrm{miss}}$.

4.2 The off-Z search regions

Additional SRs ("edge" and "slepton") are defined targeting models without on-shell Z bosons in the final state. The edge SRs are designed for signals with several jets in the final state and with a kinematic edge in the dilepton invariant mass distribution. The slepton SRs do not require significant hadronic activity in the final state.

4.2.1 Edge search regions

Events in the edge SR must have at least two jets, $p_{\mathrm{T}}^{\mathrm{miss}} > 150$ or 200 GeV, and $M_{\mathrm{T2}}(\ell\ell) > 80$ GeV, to reject Drell–Yan and $\mathrm{t\bar{t}}$ events. In order to search for a kinematic edge in the $m_{\ell\ell}$ spectrum, two different approaches are used. The first approach is based on a kinematic fit of the $m_{\ell\ell}$ distribution in events with $p_{\mathrm{T}}^{\mathrm{miss}} > 200$ GeV, as described in Section 6. In the second approach, we perform a counting experiment in events with $p_{\mathrm{T}}^{\mathrm{miss}} > 150$ GeV, distributed across 28 disjoint regions, as described below. First, we define seven bins in $m_{\ell\ell}$, excluding the region $86 < m_{\ell\ell} < 96$ GeV, in order to be able to probe different positions of a potential kinematic edge. For each $m_{\ell\ell}$ bin, events are further categorized according to the b-tagged jet multiplicity, counting b-tagged jets with $p_{\mathrm{T}} > 25$ GeV. Events are also categorized as $\mathrm{t\bar{t}}$-like or non-$\mathrm{t\bar{t}}$-like, based on a likelihood discriminant that exploits the different kinematic properties of $\mathrm{t\bar{t}}$ events with respect to a range of potential BSM contributions. To this purpose, we use four observables, $p_{\mathrm{T}}^{\mathrm{miss}}$, $p_{\mathrm{T}}^{\ell\ell}$, $|\Delta\phi^{\ell\ell}|$, and $\sum m_{\ell\mathrm{b}}$, as inputs to a Bayes discriminator in the form of probability density functions.

The $\sum m_{\ell\mathrm{b}}$ variable is defined as the sum of the invariant masses of two combinations, each constructed using a lepton and a jet. Priority is given to combinations consisting of a lepton and a b-tagged jet. However, if there are no b-tagged jets in the event, we use jets without b tags. The first lepton-jet combination is selected as the one with the minimum invariant mass. The second combination is obtained by repeating the same procedure, after the exclusion of the already selected lepton and jet.

The likelihood is constructed from probability density functions for each observable derived in a DF CR enriched in $t\bar{t}$ events. We use a sum of two exponential distributions for p_T^{miss}, a third-order polynomial for $|\Delta\phi^{\ell\ell}|$, and Crystal Ball (CB) functions for both $p_T^{\ell\ell}$ and $\sum m_{\ell b}$. The negative logarithm of the likelihood is then taken as the discriminator value used to categorize that event as $t\bar{t}$-like or non-$t\bar{t}$-like.

4.2.2 Slepton search regions

The slepton SRs target BSM signatures with two leptons, significant p_T^{miss} ($p_T^{miss} > 100\,GeV$), no b-tagged jets, and moderate hadronic activity ($n_j < 2$ with a 25 GeV p_T threshold used in jet counting). The threshold on the highest p_T lepton is raised from the baseline requirement of 25 GeV to 50 GeV. In addition, $m_{\ell\ell}$ is required be smaller than 65 GeV or larger than 120 GeV and $M_{T2}(\ell\ell)$ must be larger than 100 GeV. Events are categorized based on the jet multiplicity ($n_j = 0$ or $n_j \geq 1$), but events with one jet are kept only if $p_T^{\ell_2}/p_T^{j_1} > 1.2$. The $n_j \geq 1$ category aims at recovering acceptance to potential BSM events characterized by moderate initial-state radiation (ISR). Events are then further split into bins of p_T^{miss}, as shown in Table 2.

Table 2: Summary of search category selections.

Strong on-Z search sample ($86 < m_{\ell\ell} < 96\,GeV$)					
Region	n_j	n_b	H_T [GeV]	$M_{T2}(\ell\ell)$ [GeV]	p_T^{miss} bins [GeV]
SRA b veto	2–3	$= 0$	> 500	> 80	[100,150,230,300,∞)
SRB b veto	4–5	$= 0$	> 500	> 80	[100,150,230,300,∞)
SRC b veto	≥ 6	$= 0$	—	> 80	[100,150,250,∞)
SRA b tag	2–3	≥ 1	> 200	> 100	[100,150,230,300,∞)
SRB b tag	4–5	≥ 1	> 200	> 100	[100,150,230,300,∞)
SRC b tag	≥ 6	≥ 1	—	> 100	[100,150,250,∞)
EW on-Z search sample ($86 < m_{\ell\ell} < 96\,GeV$)					
Region	n_j ($n_{W^\pm/Z}^{boosted}$)	n_b	Dijet mass [GeV]	M_{T2} [GeV]	p_T^{miss} bins [GeV]
Boosted VZ	< 2 (≥ 1)	$= 0$	—	—	[100,200,300,400,500,∞)
Resolved VZ	≥ 2	$= 0$	$m_{jj} < 110$	$M_{T2}(\ell\ell) > 80$	[100,150,250,350,∞)
HZ	≥ 2	$= 2$	$m_{bb} < 150$	$M_{T2}(\ell b \ell b) > 200$	[100,150,250,∞)
Slepton search sample ($m_{\ell\ell} < 65$ or $m_{\ell\ell} > 120\,GeV$)					
Region	n_j	n_b	$p_T^{\ell_2}/p_T^{j_1}$	M_{T2} [GeV]	p_T^{miss} bins [GeV]
Slepton jet-less	$= 0$	$= 0$	—	$M_{T2}(\ell\ell) > 100$	[100,150,225,300,∞)
Slepton with jets	> 0	$= 0$	> 1.2	$M_{T2}(\ell\ell) > 100$	[100,150,225,300,∞)
Edge search sample ($m_{\ell\ell} < 86$ or $m_{\ell\ell} > 96\,GeV$)						
Region	n_j	n_b	$M_{T2}(\ell\ell)$ [GeV]	p_T^{miss} [GeV]	$t\bar{t}$ likelihood	$m_{\ell\ell}$ bins [GeV]
Edge fit	≥ 2	—	> 80	> 200	—	> 20
$t\bar{t}$-like b veto	≥ 2	$= 0$	> 80	> 150	< 24	[20,60,86]+[96,150,200,300,400,∞)
non-$t\bar{t}$-like b veto	≥ 2	$= 0$	> 80	> 150	> 24	[20,60,86]+[96,150,200,300,400,∞)
$t\bar{t}$-like b tag	≥ 2	≥ 1	> 80	> 150	< 24	[20,60,86]+[96,150,200,300,400,∞)
non-$t\bar{t}$-like b tag	≥ 2	≥ 1	> 80	> 150	> 24	[20,60,86]+[96,150,200,300,400,∞)

5 Standard model background predictions

Three sources of SM backgrounds contribute to the SRs used in this search. The first consists of flavor-symmetric backgrounds, from SM processes where SF and DF lepton pairs are produced at the same rate. The dominant process contributing to such category is $t\bar{t}$ production. Additional contributions arise from WW, $Z/\gamma^* \to \tau^+\tau^-$ and tW production, as well as from events with leptons from hadron decays. Flavor-symmetric backgrounds are predicted using DF data samples.

The second source of backgrounds results from DY+jets events with significant instrumental p_T^{miss}. This background is estimated from photon data samples in combination with CRs enriched in DY+jets events.

The third type of SM backgrounds consists of processes yielding final states with a SF lepton pair produced in decay of a Z/γ^* boson and neutrinos (ν) produced in the decay of a W or Z boson. The main processes contributing here are WZ and ZZ production. Rarer processes, such as $t\bar{t}Z$ production, also contribute in certain SRs. These backgrounds are referred to as Z+ν backgrounds and are estimated from simulation. The prediction is validated in dedicated data control samples.

5.1 Flavor-symmetric backgrounds

As already mentioned, the estimation of the flavor-symmetric backgrounds relies on the fact that in such processes DF and SF events are produced at the same rate. CRs are defined in data with the same selections as the corresponding SRs, but requiring the presence of a DF lepton pair instead of a SF pair. The background contribution in the SR is then predicted by means of a transfer factor, denoted by $R_{\mathrm{SF/DF}}$, that accounts for differences in reconstruction, identification and trigger efficiencies between DF and SF events. These differences are caused by differences in efficiencies between electrons and muons. The transfer factor consists of the product of two correction factors, which are determined in CR in data.

The first correction factor, $r_{\mu/\mathrm{e}}$, is the ratio of muon and electron reconstruction and identification efficiencies, and is measured in a region enriched in DY events, requiring two SF leptons, at least two jets, $p_{\mathrm{T}}^{\mathrm{miss}} < 50\,\mathrm{GeV}$ and $60 < m_{\ell\ell} < 120\,\mathrm{GeV}$. Assuming that the efficiency for each of the two leptons in the event is independent of the other lepton, $r_{\mu/\mathrm{e}}$ can be defined as $r_{\mu/\mathrm{e}} = \sqrt{N_{\mu^+\mu^-}/N_{\mathrm{e}^+\mathrm{e}^-}}$. The $r_{\mu/\mathrm{e}}$ factor is parametrized as a function of the lepton p_{T} and η by the following empirical functional form:

$$r_{\mu/\mathrm{e}}(\ell) = r^0_{\mu/\mathrm{e}} \cdot f\left(p_{\mathrm{T}}(\ell)\right) \cdot g\left(\eta(\ell)\right), \tag{2}$$

where

$$f(p_{\mathrm{T}}) = (a_1 + b_1/p_{\mathrm{T}}), \tag{3}$$

and

$$g(\eta) = a_2 + \begin{cases} 0 & |\eta| < 1.6 \\ c_1 \cdot (\eta - 1.6)^2 & \eta > 1.6 \\ c_2 \cdot (\eta + 1.6)^2 & \eta < -1.6 \end{cases}. \tag{4}$$

The constants a_1, a_2, b_1, c_1, and c_2 are extracted in a fit of the $r_{\mu/\mathrm{e}}$ distribution to data as a function of η and p_{T}. These values, shown in Table 3, are obtained separately for each data taking year, and were found to be statistically consistent with those predicted from simulation. A larger dependency on η is observed in the $r_{\mu/\mathrm{e}}$ factor in 2016 and 2017 data which is caused by a transparency loss of the ECAL that affected the detector performance and was accounted for in the 2018 data reconstruction. We assign systematic uncertainties of 5% to the measured $r_{\mu/\mathrm{e}}$ value and an additional 5% for each of its p_{T} and η parametrizations in order to cover for potential residual kinematic dependencies.

Neglecting differences in trigger efficiencies, $r_{\mu/\mathrm{e}}$ can be used to estimate the number of flavor-symmetric ($\mathrm{e}^{\pm}\mathrm{e}^{\mp}$ and $\mu^{\pm}\mu^{\mp}$) events from the observed number of DF events (N_{DF}) in the DF CR, as follows: $N^{\mathrm{est.}}_{\mathrm{e}^{\pm}\mathrm{e}^{\mp}} = (1/2)(r_{\mu/\mathrm{e}}(p^{\mathrm{e}}_{\mathrm{T}}, \eta^{\mathrm{e}})^{-1})N_{\mathrm{DF}}$ and $N^{\mathrm{est.}}_{\mu^{\pm}\mu^{\mp}} = (1/2)(r_{\mu/\mathrm{e}}(p^{\mu}_{\mathrm{T}}, \eta^{\mu}))N_{\mathrm{DF}}$.

A further correction factor, R_{T}, defined as $R_{\mathrm{T}} = \sqrt{\epsilon^T_{\mu\mu}\epsilon^T_{\mathrm{ee}}}/\epsilon^T_{\mathrm{e}\mu}$, is then used to account for differences between SF and DF dilepton trigger efficiencies. Such efficiencies are measured in data and are found to be 85–95%, depending on the lepton flavor and on the data taking period. The resulting R_{T} coefficient is measured to be 1.03–1.05, with an uncertainty of 4–5%.

Table 3: Summary of the $r_{\mu/e}$ parameters obtained by fitting the lepton p_T and η, in a DY-enriched CR for the different data taking years. Only statistical uncertainties are tabulated.

year	$r^0_{\mu/e}$	a_1	b_1	a_2	c_1	c_2
2016	1.277±0.001	1.493±0.008	6.135±0.364	0.600±0.001	0.356±0.022	0.476±0.024
2017	1.226±0.001	1.356±0.008	6.665±0.325	0.647±0.002	0.462±0.024	0.690±0.027
2018	1.234±0.001	1.437±0.006	3.870±0.266	0.653±0.001	0.097±0.015	0.099±0.015

The transfer factor $R_{SF/DF}$, used to predict SF events from DF events, is finally defined as:

$$R_{SF/DF} = (1/2)(r_{\mu/e}(p_T^{\mu}, \eta^{\mu}) + r_{\mu/e}(p_T^{e}, \eta^{e})^{-1})R_T. \quad (5)$$

The background estimation method is validated in data from a region enriched in flavor-symmetric $t\bar{t}$ events. This region is defined by requiring a SF lepton pair, exactly two jets, and $100 < p_T^{miss} < 150\,GeV$. Events with $70 < m_{\ell\ell} < 110\,GeV$ are rejected in order to reduce the contribution from DY. Figure 3 compares the prediction from a DF selection to the SF data in this region as a function of different kinematic variables. Agreement within uncertainties is observed, thus validating the background estimation method.

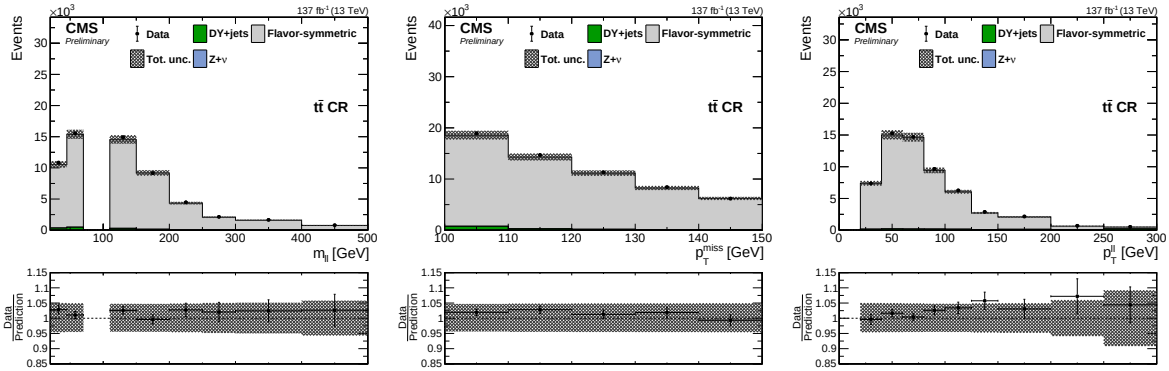

Figure 3: Distributions for (left) $m_{\ell\ell}$, (middle) p_T^{miss} and (right) $p_T^{\ell\ell}$ in a $t\bar{t}$-enriched CR in data. The data-driven flavor-symmetric background prediction (gray solid histogram) is compared to data (black marker). Other backgrounds are estimated directly from simulation (green and blue solid histograms). The uncertainty band includes systematic and statistical uncertainties in the prediction.

The statistical uncertainty arising from the limited size of the DF control sample represents the dominant contribution to the total uncertainty in the flavor-symmetric background prediction. For the estimation of this background in the on-Z SRs, where $86 < m_{\ell\ell} < 96\,GeV$, the $m_{\ell\ell}$ requirement in the DF control sample is relaxed to $m_{\ell\ell} > 20\,GeV$, and an additional multiplicative factor, $\kappa = N^{DF}(86 < m_{\ell\ell} < 96\,GeV)/N^{DF}(m_{\ell\ell} > 20\,GeV)$, is used to account for the different $m_{\ell\ell}$ selection in CRs and SRs. The factor κ is determined in dedicated DF CRs in data, defined by relaxing or merging a subset of the selection requirements described in Section 4. The regions considered are SRA, SRB and SRC, strong SRs, the HZ, and resolved VZ SRs. The boosted VZ is also considered, relaxing the veto of additional jets. In these regions, κ is is measured to be in the range 0.045–0.067. We assign a systematic uncertainty of 20% to the value of κ in order to cover for potential kinematic dependencies.

5.2 Drell–Yan+jets backgrounds

The contribution of DY+jets events to the SRs mainly arises from mismeasurements of the momenta of the reconstructed objects, affecting $\vec{p}_{\mathrm{T}}^{\,\mathrm{miss}}$. In regions where jets in the final state are required, instrumental $p_{\mathrm{T}}^{\mathrm{miss}}$ mostly arises from jet energy mismeasurements, and the $p_{\mathrm{T}}^{\mathrm{miss}}$ "templates" method [15–18] is used to estimate the resulting background contribution. In the slepton SRs, since only jets with low p_{T} are present, we use a different estimation method, exploiting a CR in data enriched in DY+jets events.

The $p_{\mathrm{T}}^{\mathrm{miss}}$ "templates" method relies on the fact that instrumental $p_{\mathrm{T}}^{\mathrm{miss}}$ in DY+jets events is caused by the limited detector resolution in measuring the p_{T} of the jets recoiling against the leptonically-decaying Z boson. Since the p_{T} resolution of leptons and photons is much better than that of jets, the $p_{\mathrm{T}}^{\mathrm{miss}}$ distribution in DY+jets events can be directly estimated from a γ+jets data sample.

Samples of γ+jets events are selected using identical jet requirements as those used in the definition of the SRs of Section 4. Note that the γ+jets samples are not affected by potential contamination from any of the BSM physics models considered in this search.

The M_{T2} variable used to select events in a number of SRs requires the presence of two visible objects and cannot be defined in the γ sample. Instead, its behavior is emulated by simulating the decay of the photon into two leptons. The decay is modeled assuming that the mother particle of the leptons has the mass of a Z boson and the momentum of the selected photon, with the angular distributions in the decay as expected at LO in perturbation theory.

The simulated leptons are used to calculate the $M_{\mathrm{T2}}(\ell\ell)$ variable in the γ+jets data sample.

Events with genuine $p_{\mathrm{T}}^{\mathrm{miss}}$ may be present in the γ+jets sample, originating from EW processes such as $\mathrm{W}^{\pm}\gamma$ production, where the $\mathrm{W}^{\pm}$ boson decays to $\ell\nu$. However, such contribution can be suppressed by rejecting events that contain additional leptons. The residual EW contamination in the γ+jets sample, which is larger at large $p_{\mathrm{T}}^{\mathrm{miss}}$, is subtracted based on simulation.

The photon p_{T} distribution in the γ+jets sample is expected to differ from that of the Z boson in DY+jets, mainly because of the different boson masses. Thus, simulation is used in each SR to correct the photon p_{T} distribution in order to match the expected Z boson p_{T} distribution. After this correction, the photon $p_{\mathrm{T}}^{\mathrm{miss}}$ template in each SR is normalized based on the observed dilepton data yield in the range $50 < p_{\mathrm{T}}^{\mathrm{miss}} < 100\,\mathrm{GeV}$, where DY+jets events dominate the data sample. Note that in order to account for potential contamination from BSM physics, the $50 < p_{\mathrm{T}}^{\mathrm{miss}} < 100\,\mathrm{GeV}$ bin in each SR is included in the signal extraction fit described in Section 8.

Several sources of uncertainty are considered for the DY+jets prediction: statistical uncertainty arising from the size of the γ+jets sample in each $p_{\mathrm{T}}^{\mathrm{miss}}$ bin, systematic uncertainty in the EW subtraction, and statistical uncertainty in the template normalization, arising from the dilepton data yield in the range $50 < p_{\mathrm{T}}^{\mathrm{miss}} < 100\,\mathrm{GeV}$. An additional systematic uncertainty is assessed by performing a closure test of the method in simulation, where the $p_{\mathrm{T}}^{\mathrm{miss}}$ distribution in DY+jets simulated events is compared to the distribution obtained by applying the background prediction method to a γ+jets simulated sample. In each $p_{\mathrm{T}}^{\mathrm{miss}}$ bin, we assign an uncertainty equal to the largest of the difference between prediction and simulated yield, and the statistical uncertainty reflecting the size of the samples. The resulting uncertainty ranges between 20 and 100% across the search bins, with the largest values obtained in bins affected by the limited size of the simulated samples.

The validity of the method is further evaluated in data control samples enriched in events with

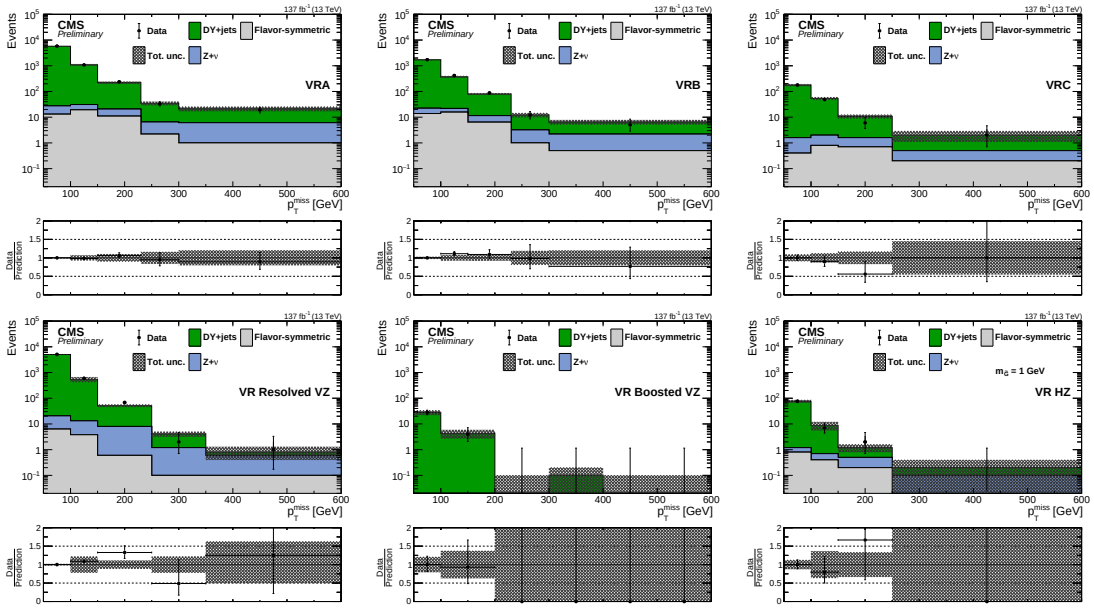

Figure 4: The $p_{\mathrm{T}}^{\mathrm{miss}}$ distribution observed in data (black markers) is compared to the background prediction (solid histograms) in the on-Z VRs. (Upper) Comparison in the strong on-Z VRs: (left) SRA, (middle) SRB, and (right) SRC. (Lower) Comparison in the EW on-Z VRs: (left) resolved VZ, (middle) boosted VZ, and (right) HZ. The uncertainty band includes systematic and statistical uncertainties in the prediction.

instrumental $p_{\mathrm{T}}^{\mathrm{miss}}$. These samples are defined by inverting the $\Delta\phi(\vec{p}_{\mathrm{T}}^{\,\mathrm{j}_{1,2}}, \vec{p}_{\mathrm{T}}^{\,\mathrm{miss}})$ selection (or $\Delta\phi(\mathrm{W}^{\pm}/\mathrm{Z}$ candidate, $\vec{p}_{\mathrm{T}}^{\,\mathrm{miss}})$, in the boosted VZ region). In addition, the b-tagged jet multiplicity categorization is removed from the on-Z strong regions, yielding a total of six validation regions (VRs) with the same $p_{\mathrm{T}}^{\mathrm{miss}}$ binning as used in the corresponding SRs. The observed $p_{\mathrm{T}}^{\mathrm{miss}}$ distribution is compared to the prediction in the VRs in Fig. 4, showing agreement within uncertainties.

The method described above is also used to predict the DY+jets background in the edge SRs, where events with $86 < m_{\ell\ell} < 96\,\mathrm{GeV}$ are rejected, and therefore the contribution from DY+jets events is expected to be small. In this case, the prediction is obtained from a region with inverted $m_{\ell\ell}$ selection, by means of a transfer factor, $r_{\mathrm{in/out}}$, defined as the ratio of the DY+jets yield in a given $m_{\ell\ell}$ bin over the yield in the range $86 < m_{\ell\ell} < 96\,\mathrm{GeV}$. The $r_{\mathrm{in/out}}$ ratio is measured in a data control sample enriched in DY+jets events, obtained by requiring at least two jets, $p_{\mathrm{T}}^{\mathrm{miss}} < 50\,\mathrm{GeV}$, and $M_{\mathrm{T2}}(\ell\ell) > 80\,\mathrm{GeV}$, after subtracting the flavor-symmetric contribution, estimated as described in Section 5.1. The $r_{\mathrm{in/out}}$ value is measured to be in the range 0.003–0.06, depending on the $m_{\ell\ell}$ bin. We assign a systematic uncertainty in $r_{\mathrm{in/out}}$ to cover for its potential dependencies on $p_{\mathrm{T}}^{\mathrm{miss}}$ and n_{j}, of 50 (100)% in $m_{\ell\ell}$ bins below (above) 150 GeV.

In the slepton SRs, the DY+jets background is estimated in each $p_{\mathrm{T}}^{\mathrm{miss}}$ bin using a data control sample enriched in DY+jets events, obtained by applying the same selection criteria as in the SRs, but inverting the selection on $m_{\ell\ell}$ ($65 < m_{\ell\ell} < 120\,\mathrm{GeV}$). The prediction is then obtained by means of a transfer factor, $r_{\mathrm{in/out}}$, which is measured in data, after relaxing the $p_{\mathrm{T}}^{\mathrm{miss}}$ and n_{j} selections applied in the SRs. The $r_{\mathrm{in/out}}$ value is measured to be 0.07, with a 50% uncertainty derived from a closure test performed in DY+jets simulated events. In order to account for potential contamination from BSM physics in the $65 < m_{\ell\ell} < 120\,\mathrm{GeV}$ region, that region is included in the signal extraction fit described in Section 8.

5.3 Backgrounds with Z bosons and genuine $p_{\mathrm{T}}^{\mathrm{miss}}$

Backgrounds from events with Z/γ^* bosons and genuine $p_{\mathrm{T}}^{\mathrm{miss}}$ such as WZ, ZZ, and $\mathrm{t\bar{t}Z}$ can be important in regions with large $p_{\mathrm{T}}^{\mathrm{miss}}$, and are estimated directly from simulation. Dedicated data control samples of trileptons and two pairs of OCSF leptons are used to determine the overall normalization and to test the modeling of WZ, $\mathrm{t\bar{t}Z}$, and ZZ in simulation. Systematic uncertainties as large as 50% are assessed for each process, to cover differences between data and simulation. In predicting the ZZ yield we also assign an additional uncertainty given by the difference between the NLO and the NNLO/NLO κ-factor described in Section 3. Finally, we include statistical uncertainties associated with the limited size of the simulated samples, and systematic uncertainties arising from the modeling of pileup, lepton reconstruction and isolation efficiencies, b tagging efficiency, ISR, and jet energy scale (JES), as well as the choice of the renormalization (μ_{R}) and factorization (μ_{F}) scales used in the event generator. The uncertainties are summarized in Table 4, together with their typical size in the various SRs.

For each data sample corresponding to the different periods of data taking (2016, 2017, and 2018), uncertainties in the luminosity measurement, ISR modeling, fast simulation $p_{\mathrm{T}}^{\mathrm{miss}}$ distributions, and trigger, b tagging and lepton efficiencies are treated as correlated across search regions. Uncertainties in the ISR modeling, fast simulation $p_{\mathrm{T}}^{\mathrm{miss}}$ distributions, jet energy scale, and trigger, b tagging and lepton efficiencies are treated as correlated also across data samples. The remaining uncertainties are taken as uncorrelated.

Table 4: Summary of the systematic uncertainties in the predicted Z+ν background yields, together with their typical sizes across the SRs.

Source of uncertainty	Uncertainty (%)
Limited size of simulated samples	1–15
Data/simulation in control regions	30–50
NNLO/NLO κ-factor (for ZZ)	10–30
Lepton efficiency	5
b tag efficiency	0–5
Jet energy scale	0–5
Pileup modeling	1–2
ISR modeling	0–2.5
μ_{R} and μ_{F} variation	1–3

6 Kinematic fit

We perform a simultaneous unbinned maximum likelihood fit of the $m_{\ell\ell}$ distributions in $\mathrm{e^{\pm}e^{\mp}}$, $\mu^{\pm}\mu^{\mp}$ and $\mathrm{e^{\pm}}\mu^{\mp}$ data to search for a kinematic edge. The fit is performed in the "edge fit" SR defined in Section 4. The functional forms used to model the signal and the two main SM background components (flavor-symmetric background and backgrounds arising from other SM processes containing a Z boson) are described below.

The flavor-symmetric background component is modeled using a Crystal Ball (CB) function, $\mathcal{P}_{\mathrm{CB}}(m_{\ell\ell})$:

$$\mathcal{P}_{\mathrm{CB}}(m_{\ell\ell}) = \begin{cases} \exp\left[-\frac{(m_{\ell\ell}-\mu_{\mathrm{CB}})^2}{2\Gamma_{\mathrm{CB}}^2}\right] & \text{if } \frac{m_{\ell\ell}-\mu_{\mathrm{CB}}}{\Gamma_{\mathrm{CB}}} < \alpha \\ A(B+\frac{m_{\ell\ell}-\mu_{\mathrm{CB}}}{\Gamma_{\mathrm{CB}}})^{-n} & \text{if } \frac{m_{\ell\ell}-\mu_{\mathrm{CB}}}{\Gamma_{\mathrm{CB}}} > \alpha \end{cases}, \tag{6}$$

where

$$A = \left(\frac{n}{|\alpha|}\right)^n \exp\left(-\frac{|\alpha|^2}{2}\right) \quad \text{and} \quad B = \frac{n}{|\alpha|} - |\alpha|. \tag{7}$$

This model has five free parameters: the overall normalization, the mean μ_{CB} and width Γ_{CB} of the Gaussian core component, the transition point α between the Gaussian core and the power law tail, and the power law parameter n.

Backgrounds containing a leptonically decaying Z boson (Z + X) are modeled with the sum of an exponential function, which describes the low-mass rise, and a Breit–Wigner function with mean and width set to the nominal Z boson values [88] convolved with a double-sided CB function, $\mathcal{P}_{\text{DSCB}}(m_{\ell\ell})$ to account for the experimental resolution:

$$\mathcal{P}_{\text{DSCB}}(m_{\ell\ell}) = \begin{cases} A_1(B_1 - \frac{m_{\ell\ell}-\mu_{\text{DSCB}}}{\Gamma_{\text{DSCB}}})^{-n_1} & \text{if } \frac{m_{\ell\ell}-\mu_{\text{DSCB}}}{\Gamma_{\text{DSCB}}} < -\alpha_1 \\ \exp\left[-\frac{(m_{\ell\ell}-\mu_{\text{DSCB}})^2}{2\Gamma_{\text{DSCB}}^2}\right] & \text{if } -\alpha_1 < \frac{m_{\ell\ell}-\mu_{\text{DSCB}}}{\Gamma_{\text{DSCB}}} < \alpha_2 \\ A_2(B_2 + \frac{m_{\ell\ell}-\mu_{\text{DSCB}}}{\Gamma_{\text{DSCB}}})^{-n_2} & \text{if } \frac{m_{\ell\ell}-\mu_{\text{DSCB}}}{\Gamma_{\text{DSCB}}} > \alpha_2 \end{cases}, \tag{8}$$

where μ_{DSCB} and Γ_{DSCB} are the mean and width, respectively, of the CB function, and α_1 and α_2 are the transition points. The model for the resonant Z +X background line shape is thus:

$$\mathcal{P}_{\text{Z+X,res}}(m_{\ell\ell}) = \int \mathcal{P}_{\text{DSCB}}(m')\mathcal{P}_{\text{BW}}(m_{\ell\ell} - m')\mathrm{d}m', \tag{9}$$

where $\mathcal{P}_{\text{BW}}$ is the Breit–Wigner function. The complete DY+jets background model then has nine free parameters.

The signal component is described by a triangular shape, convolved with a Gaussian distribution to account for the experimental resolution:

$$\mathcal{P}_{\text{S}}(m_{\ell\ell}) \propto \frac{1}{\sqrt{2\pi}\Gamma_{\ell\ell}} \int_0^{m_{\ell\ell}^{\text{edge}}} y \exp\left[-\frac{(m_{\ell\ell} - y)^2}{2\Gamma_{\ell\ell}^2}\right] \mathrm{d}y. \tag{10}$$

The signal model has two free parameters: the fitted signal yield and the position of the kinematic endpoint, $m_{\ell\ell}^{\text{edge}}$.

In an initial step, a fit to data is performed in a DY+jets-enriched CR with at least two jets, $M_{\text{T2}} > 80\,\text{GeV}$ and $p_{\text{T}}^{\text{miss}} < 50\,\text{GeV}$, separately for $\text{e}^{\pm}\text{e}^{\mp}$ and $\mu^{\pm}\mu^{\mp}$ events, in order to determine the shape parameters for backgrounds containing a Z boson. The final fit is then performed simultaneously to the invariant mass distributions in the e^{+}e^{-}, $\mu^{+}\mu^{-}$ and $\text{e}^{\pm}\mu^{\mp}$ data samples. The model of the flavor-symmetric background is varied consistently in the SF and DF samples. The relative normalization of SF and DF events is given by the $R_{\text{SF/DF}}$ factor, which is treated as a nuisance parameter, constrained by a Gaussian prior with a mean value and standard deviation as determined in Section 5.1. In total, the final fit has ten parameters: a normalization parameter for each of the three fit components, four parameters for the shape of the flavor-symmetric background, $R_{\text{SF/DF}}$, the relative fraction of dielectron and dimuon events in the flavor-symmetric prediction, and the position of the signal edge. Out of these, only $R_{\text{SF/DF}}$ is constrained, while the others are treated as free parameters.

7 Results

The observed data yields in each SR are compared to the SM predictions, for the on-Z, edge and slepton SRs. For the edge search, a fit is additionally performed to the $m_{\ell\ell}$ distribution in

data to search for a kinematic edge in the $m_{\ell\ell}$ spectrum, as described in the previous Section.

7.1 Results for the on-Z search regions

The results for the strong-production on-Z search regions are summarized in Table 5. The corresponding $p_{\mathrm{T}}^{\mathrm{miss}}$ distributions are shown in Fig. 5. No significant deviations are observed with respect to SM background predictions. The largest disagreement corresponds to one of the SRA b tag categories, in which 42 events are observed and 31.4 ± 3.8 background events are expected, corresponding to a local significance of 1.4 standard deviations (s.d.).

The results for the EW on-Z search regions are summarized in Table 6. The corresponding $p_{\mathrm{T}}^{\mathrm{miss}}$ distributions are shown in Fig. 6. The observed data yields are consistent with the SM background predictions. The largest discrepancy between data and prediction occurs in the highest $p_{\mathrm{T}}^{\mathrm{miss}}$ bin of the resolved VZ regions, where 2 events are observed while 6.3 ± 2.2 are predicted, corresponding to a local significance of -1.2 s.d.

7.2 Results for the edge search regions

Comparisons between the SM predictions and the observed yields in the 28 search regions are summarized in Table 7. A graphical representation of the same results is displayed in Fig. 7.

We find agreement between observed data yields and SM predictions in all SRs. The largest deviation is observed in the $\mathrm{t\bar{t}}$-like region with $300 < m_{\ell\ell} < 400\,\mathrm{GeV}$ and $n_{\mathrm{b}} \geq 1$, with a deficit of data corresponding to a local significance of -2.4 standard deviations.

The dilepton mass distributions and the results of the kinematic fit are shown in Fig. 8, while Table 8 presents a summary of the fit results. A best-fit signal yield of 27 ± 22 events is obtained when evaluating the signal hypothesis in the edge fit search region, with a fitted edge position of $m_{\ell\ell} = 293.4^{+12.6}_{-0.0}\,\mathrm{GeV}$. To test the compatibility of this result with the background-only hypothesis, we estimate the global p-value [89] of the result using the test statistic $-2\ln Q$, where Q denotes the ratio of the fitted likelihood value for the signal+background hypothesis to the background-only hypothesis. The test statistic $-2\ln Q$ is evaluated in data and compared to the corresponding quantity computed using a large sample of background-only pseudo-experiments where the edge position is not fixed to any particular value. The resulting p-value is interpreted as the one-sided tail probability of a Gaussian distribution, and corresponds to an excess in the observed data yields compared to the SM background prediction with a global significance of 0.7 s.d. If unphysical negative signal yields are permitted, the best fit corresponds to a negative signal yield with an edge position of 34.4 GeV and a global significance of 1.8 s.d.

7.3 Results in the slepton search regions

The $p_{\mathrm{T}}^{\mathrm{miss}}$ distribution of data events in the slepton search regions is shown together with the SM background predictions in Fig. 9. Results are also summarized in Table 9. The observed data yields are consistent with the SM predictions. The largest discrepancy between data and SM prediction is observed in the highest $p_{\mathrm{T}}^{\mathrm{miss}}$ bin of the search region without jets, where 17 events are observed and 9.3 ± 2.3 are predicted, corresponding to a local significance of 1.6 standard deviations.

Table 5: Predicted and observed event yields in the strong-production on-Z search regions, for each $p_{\mathrm{T}}^{\mathrm{miss}}$ bin, as defined in Table 2, before the fits to data described in Section 8. Uncertainties include both statistical and systematic sources. The $p_{\mathrm{T}}^{\mathrm{miss}}$ template prediction in each search region is normalized to the first $p_{\mathrm{T}}^{\mathrm{miss}}$ bin of each distribution in data.

Category	SM processes					
SRA b veto	$p_{\mathrm{T}}^{\mathrm{miss}}$ [GeV]	50–100	100–150	150–230	230–300	>300
	DY+jets	1253 ± 41	153 ± 16	22.0 ± 4.9	0.9 ± 0.8	2.9 ± 3.0
	Flavor-symmetric	$1.6^{+0.5}_{-0.5}$	$2.1^{+0.6}_{-0.6}$	$1.4^{+0.5}_{-0.5}$	$0.6^{+0.3}_{-0.3}$	$0.6^{+0.2}_{-0.2}$
	Z+ν	6.4 ± 1.2	4.9 ± 0.9	5.3 ± 1.0	2.7 ± 0.5	6.2 ± 1.2
	Total background	1261^{+41}_{-41}	160^{+16}_{-16}	$28.8^{+5.0}_{-5.0}$	$4.2^{+1.0}_{-1.0}$	$9.6^{+3.2}_{-3.2}$
	Data	1261	186	27	5	14
SRA b tag	$p_{\mathrm{T}}^{\mathrm{miss}}$ [GeV]	50–100	100–150	150–230	230–300	>300
	DY+jets	602.2 ± 28	99.9 ± 9.3	12.3 ± 2.6	2.2 ± 1.6	1.1 ± 1.0
	Flavor-symmetric	$7.9^{+1.8}_{-1.8}$	$19.7^{+4.4}_{-4.4}$	$10.6^{+2.4}_{-2.4}$	$1.4^{+0.4}_{-0.4}$	$0.3^{+0.2}_{-0.2}$
	Z+ν	5.8 ± 0.9	8.1 ± 1.2	8.4 ± 1.2	2.8 ± 0.5	2.6 ± 0.6
	Total background	616^{+28}_{-28}	128^{+10}_{-10}	$31.4^{+3.8}_{-3.8}$	$6.3^{+1.7}_{-1.7}$	$4.1^{+1.2}_{-1.2}$
	Data	616	148	42	10	4
SRB b veto	$p_{\mathrm{T}}^{\mathrm{miss}}$ [GeV]	50–100	100–150	150–230	230–300	>300
	DY+jets	696 ± 31	103.6 ± 7.1	11.2 ± 2.1	0.6 ± 0.6	1.0 ± 0.9
	Flavor-symmetric	$1.2^{+0.4}_{-0.4}$	$2.4^{+0.7}_{-0.7}$	$1.0^{+0.3}_{-0.4}$	$0.6^{+0.3}_{-0.3}$	$0.1^{+0.2}_{-0.1}$
	Z+ν	2.6 ± 0.5	2.3 ± 0.4	3.5 ± 0.6	0.9 ± 0.2	1.9 ± 0.4
	Total background	700^{+31}_{-31}	$108.2^{+7.1}_{-7.1}$	$15.7^{+2.3}_{-2.3}$	$2.2^{+0.7}_{-0.7}$	$3.0^{+1.0}_{-1.0}$
	Data	700	108	18	2	3
SRB b tag	$p_{\mathrm{T}}^{\mathrm{miss}}$ [GeV]	50–100	100–150	150–230	230–300	>300
	DY+jets	215 ± 16	48 ± 16	10.7 ± 3.8	1.9 ± 1.3	0.4 ± 0.5
	Flavor-symmetric	$4.5^{+1.1}_{-1.2}$	$9.3^{+2.2}_{-2.2}$	$5.3^{+1.3}_{-1.3}$	$1.0^{+0.3}_{-0.4}$	$0.1^{+0.2}_{-0.1}$
	Z+ν	6.0 ± 1.1	7.9 ± 1.4	6.6 ± 1.2	2.4 ± 0.4	1.6 ± 0.3
	Total background	225^{+16}_{-16}	65^{+16}_{-16}	$22.7^{+4.2}_{-4.2}$	$5.3^{+1.4}_{-1.4}$	$2.1^{+0.6}_{-0.6}$
	Data	225	69	17	3	5
SRC b veto	$p_{\mathrm{T}}^{\mathrm{miss}}$ [GeV]	50–100	100–150	150–250	>250	
	DY+jets	135 ± 14	28.8 ± 5.6	1.7 ± 0.5	0.2 ± 0.2	
	Flavor-symmetric	$0.2^{+0.1}_{-0.1}$	$0.3^{+0.2}_{-0.2}$	$0.2^{+0.1}_{-0.1}$	$0.0^{+0.1}_{-0.0}$	
	Z+ν	0.4 ± 0.1	0.6 ± 0.2	0.5 ± 0.2	0.4 ± 0.1	
	Total background	135^{+14}_{-14}	$29.7^{+5.6}_{-5.6}$	$2.4^{+0.6}_{-0.6}$	$0.6^{+0.3}_{-0.3}$	
	Data	135	19	5	1	
SRC b tag	$p_{\mathrm{T}}^{\mathrm{miss}}$ [GeV]	50–100	100–150	150–250	>250	
	DY+jets	39.6 ± 7.1	8.9 ± 2.0	2.0 ± 0.7	0.0 ± 0.2	
	Flavor-symmetric	$0.4^{+0.3}_{-0.3}$	$0.7^{+0.4}_{-0.4}$	$0.8^{+0.5}_{-0.5}$	$0.1^{+0.1}_{-0.1}$	
	Z+ν	1.0 ± 0.2	1.0 ± 0.2	1.0 ± 0.2	0.6 ± 0.2	
	Total background	$41.0^{+7.1}_{-7.1}$	$10.7^{+2.1}_{-2.1}$	$3.8^{+0.9}_{-0.9}$	$0.7^{+0.2}_{-0.2}$	
	Data	41	14	5	1	

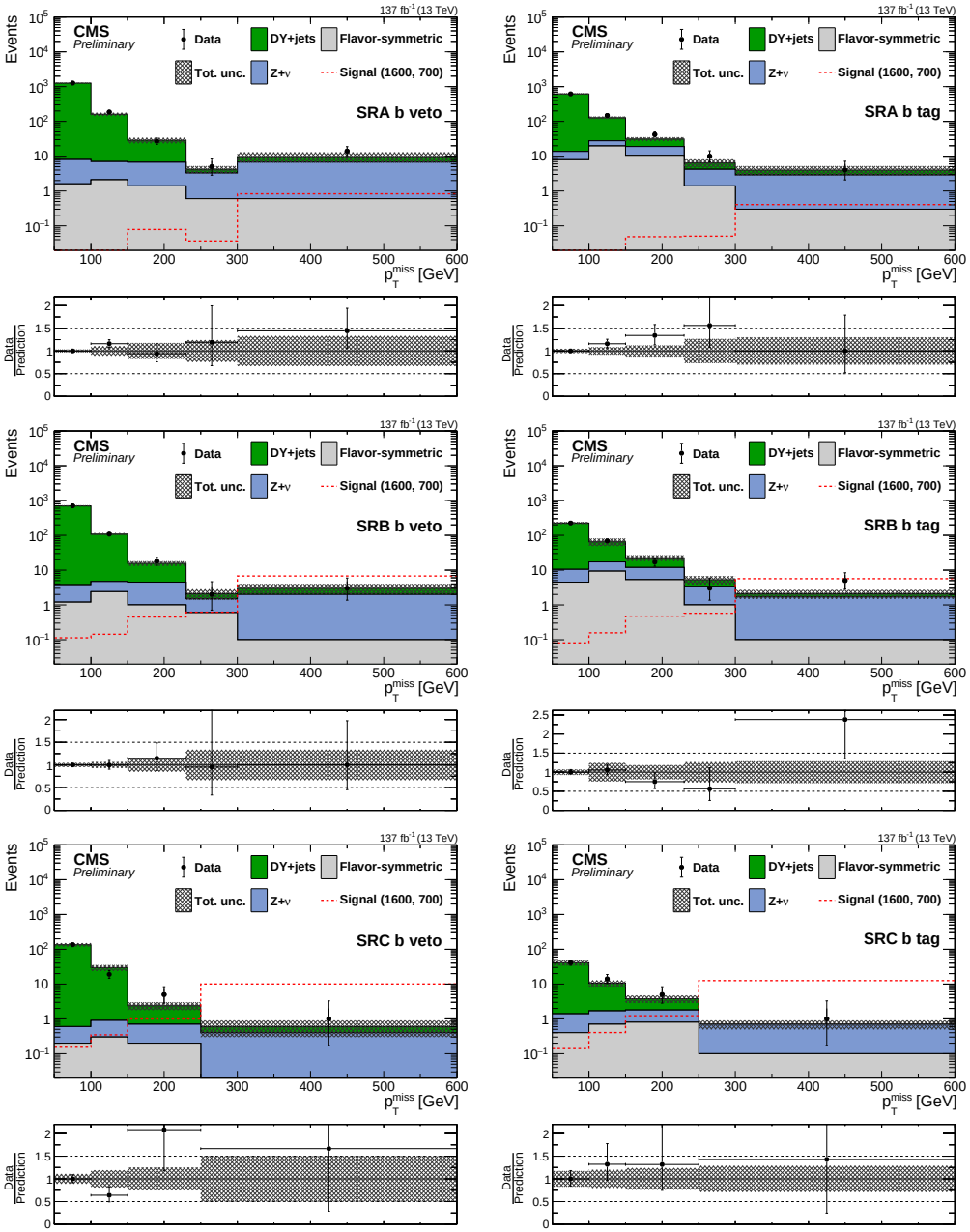

Figure 5: The $p_{\mathrm{T}}^{\mathrm{miss}}$ distribution in data is compared to the SM background prediction in the strong-production on-Z (upper) SRA, (middle) SRB, and (lower) SRC search regions, for (left) the b veto and (right) b tag categories, before the fits to data described in Section 8. The lower panel of each plot shows the ratio of observed data to the SM prediction in each $p_{\mathrm{T}}^{\mathrm{miss}}$ bin. The hashed band in the upper panels shows the total uncertainty in the background prediction, including statistical and systematic sources. The signal $p_{\mathrm{T}}^{\mathrm{miss}}$ distributions correspond to the gluino pair production model, with the gluino having a mass of 1600 GeV and $\widetilde{\chi}_1^0$ having a mass of 700 GeV. The $p_{\mathrm{T}}^{\mathrm{miss}}$ template prediction in each search region is normalized to the first $p_{\mathrm{T}}^{\mathrm{miss}}$ bin of each distribution in data.

Table 6: Predicted and observed event yields in the EW on-Z search regions, for each $p_{\mathrm{T}}^{\mathrm{miss}}$ bin, as defined in Table 2, before the fits to data described in Section 8. Uncertainties include both statistical and systematic sources. The $p_{\mathrm{T}}^{\mathrm{miss}}$ template prediction in each search region is normalized to the first $p_{\mathrm{T}}^{\mathrm{miss}}$ bin of each distribution in data.

Category	SM processes						
Boosted VZ	$p_{\mathrm{T}}^{\mathrm{miss}}$ [GeV]	50–100	100–200	200–300	300–400	400–500	>500
	DY+jets	84 ± 15	2.1 ± 0.9	0.0 ± 0.5	0.0 ± 0.0	0.0 ± 0.0	0.0 ± 0.0
	Flavor-symmetric	$0.3^{+0.2}_{-0.2}$	$0.3^{+0.2}_{-0.2}$	$0.3^{+0.2}_{-0.2}$	$0.2^{+0.2}_{-0.1}$	$0.0^{+0.1}_{-0.0}$	$0.1^{+0.1}_{-0.1}$
	Z+ν	0.2 ± 0.2	0.5 ± 0.2	0.3 ± 0.1	0.1 ± 0.1	0.0 ± 0.0	0.1 ± 0.1
	Total background	84^{+16}_{-16}	$2.9^{+0.9}_{-0.9}$	$0.6^{+0.5}_{-0.5}$	$0.3^{+0.2}_{-0.1}$	$0.0^{+0.1}_{-0.0}$	$0.2^{+0.1}_{-0.1}$
	Data	84	6	1	0	0	0
Resolved VZ	$p_{\mathrm{T}}^{\mathrm{miss}}$ [GeV]	50–100	100–150	150–250	250–350	>350	
	DY+jets	3613 ± 80	394 ± 46	21 ± 18	1.7 ± 2.4	1.8 ± 1.9	
	Flavor-symmetric	$10.7^{+3.0}_{-2.9}$	$15.4^{+4.2}_{-4.2}$	$5.1^{+1.5}_{-1.5}$	$0.5^{+0.2}_{-0.2}$	$0.3^{+0.2}_{-0.2}$	
	Z+ν	24.0 ± 4.1	29.5 ± 5.6	32.2 ± 6.5	9.7 ± 2.2	4.2 ± 1.1	
	Total background	3648^{+80}_{-80}	439^{+47}_{-47}	58^{+19}_{-19}	$11.9^{+3.2}_{-3.2}$	$6.3^{+2.2}_{-2.2}$	
	Data	3648	461	69	7	2	
HZ	$p_{\mathrm{T}}^{\mathrm{miss}}$ [GeV]	50–100	100–150	150–250	>250		
	DY+jets	163 ± 15	10.8 ± 4.1	1.3 ± 2.5	0.1 ± 0.3		
	Flavor-symmetric	$3.9^{+1.4}_{-1.4}$	$3.6^{+1.3}_{-1.3}$	$3.3^{+1.2}_{-1.2}$	$0.7^{+0.3}_{-0.3}$		
	Z+ν	1.3 ± 0.3	1.1 ± 0.2	1.0 ± 0.2	0.3 ± 0.1		
	Total background	168^{+15}_{-15}	$15.6^{+4.3}_{-4.3}$	$5.6^{+2.8}_{-2.8}$	$1.2^{+0.4}_{-0.4}$		
	Data	168	14	5	0		

8 Interpretation of the results

The results are interpreted in the context of models of BSM physics presented in Section 1. Maximum likelihood fits to the data in the SRs and CRs (for the latter, only if indicated in Section 5) are performed under either background-only or signal+background hypotheses. The uncertainties in the modeling of the backgrounds, summarized below, are inputs to the fitting procedure. The likelihoods are constructed as the product of Poisson probability density functions, one for each search region, with additional log-normal constraint terms that account for the uncertainties in the background predictions and, if considered, in the signal yields. When a CR is included in the fit, the background and signal normalizations determined from the CR itself are parametrized as freely floating parameters. This allows to account for the possible presence of signal events in the CRs (signal contamination).

The signal+background fits are used to set 95% confidence level (CL) upper limits on the production cross sections of the considered signal models. We employ a modified frequentist approach, using the $\mathrm{CL_s}$ criterion and relying on asymptotic approximations, to calculate the distribution of the profile likelihood test-statistic [90–93]. The limits are then used, together with the theoretical cross section calculations, to exclude ranges of masses for the BSM particles involved in each signal model.

8.1 Systematic uncertainties in the signal yield

We include uncertainties in the expected signal yields for all the SMSs under consideration, as summarized in Table 10. The uncertainties in the luminosity measurement are 2.5% for data collected in 2016 and 2018, and 2.3% for data collected in 2017 [94–96]. We include uncertainties in the lepton trigger, identification, and isolation efficiencies, in the b tagging efficiency and in the mistaggin probability. Additional uncertainties arise from the potential mismodeling of pileup, ISR and JES, from the choice of the μ_{R} and μ_{F} scales used in the event generator, and

Table 7: Predicted and observed yields in each bin of the edge search counting experiment, as defined in Table 2, before the fits to data described in Section 8. Uncertainties include statistical and systematic sources.

n_b	$m_{\ell\ell}$ range [GeV]	Flavor-symmetric	DY+jets	Z+ν	Total background	Data
			$t\bar{t}$-like			
	20–60	286^{+19}_{-18}	6.1±3.8	10.8±3.1	304^{+20}_{-19}	277
	60–86	163^{+14}_{-13}	12.3±7.6	42±12	217^{+20}_{-19}	251
	96–150	187^{+15}_{-14}	17±11	34±9	238^{+21}_{-20}	265
	150–200	102^{+12}_{-11}	1.7±1.8	2.5±0.8	106^{+12}_{-11}	77
	200–300	$53.4^{+8.7}_{-7.6}$	1.3±1.3	2.3±0.8	$57.0^{+8.8}_{-7.8}$	69
	300–400	$19.5^{+5.8}_{-4.6}$	0.3±0.3	0.7±0.3	$20.5^{+5.8}_{-4.7}$	24
	>400	$8.5^{+4.2}_{-3.0}$	0.5±0.5	1.3±0.5	$10.3^{+4.3}_{-3.1}$	7
$=0$			non-$t\bar{t}$-like			
	20-60	$2.1^{+2.7}_{-1.3}$	2.4±1.5	2.7±0.9	$7.1^{+3.2}_{-2.2}$	4
	60–86	$0.0^{+1.8}_{-0.0}$	4.8±3.0	8.3±2.5	$13.1^{+4.3}_{-3.9}$	13
	96–150	$4.2^{+3.3}_{-2.0}$	6.6±4.1	11.8±3.3	$22.6^{+6.2}_{-5.7}$	23
	150–200	$5.1^{+3.5}_{-2.2}$	0.6±0.7	1.3±0.5	$7.1^{+3.6}_{-2.4}$	3
	200–300	$4.1^{+3.3}_{-2.0}$	0.5±0.5	0.8±0.3	$5.4^{+3.4}_{-2.1}$	9
	300–400	$4.2^{+3.4}_{-2.1}$	0.1±0.1	0.8±0.4	$5.1^{+3.4}_{-2.1}$	6
	>400	$3.1^{+3.0}_{-1.7}$	0.2±0.2	0.9±0.3	$4.2^{+3.1}_{-1.7}$	8
			$t\bar{t}$-like			
	20–60	1432^{+48}_{-47}	3.8±2.4	1.9±0.6	1438^{+48}_{-47}	1427
	60–86	936^{+37}_{-36}	7.7±4.9	14.3±3.6	958^{+37}_{-37}	916
	96–150	897^{+36}_{-35}	10.7±6.8	10.9±2.8	918^{+37}_{-36}	918
	150–200	330^{+20}_{-19}	1.0±1.1	0.2±0.1	332^{+20}_{-19}	349
	200–300	227^{+17}_{-16}	0.8±0.8	0.1±0.0	228^{+17}_{-16}	235
	300–400	$76.3^{+10}_{-9.1}$	0.2±0.2	0.0±0.0	$76.5^{+10}_{-9.1}$	49
	>400	$25.2^{+6.3}_{-5.2}$	0.3±0.3	0.3±0.3	$25.8^{+6.3}_{-5.2}$	25
≥ 1			non-$t\bar{t}$-like			
	20-60	$5.2^{+3.5}_{-2.3}$	1.5±0.9	0.6±0.3	$7.3^{+3.7}_{-2.5}$	2
	60–86	$1.0^{+2.3}_{-0.8}$	3.0±1.9	3.8±1.0	$7.8^{+3.2}_{-2.3}$	7
	96–150	$4.3^{+3.4}_{-2.1}$	4.2±2.6	3.0±0.8	$11.5^{+4.4}_{-3.4}$	12
	150–200	$4.1^{+3.3}_{-2.0}$	0.4±0.4	0.1±0.0	$4.6^{+3.3}_{-2.1}$	7
	200–300	$2.4^{+3.2}_{-1.6}$	0.3±0.3	0.1±0.0	$2.7^{+3.2}_{-1.7}$	5
	300–400	$1.1^{+2.4}_{-0.9}$	0.1±0.1	0.0±0.0	$1.2^{+2.4}_{-0.9}$	2
	>400	$0.9^{+2.1}_{-0.9}$	0.1±0.1	0.2±0.2	$1.2^{+2.1}_{-0.9}$	1

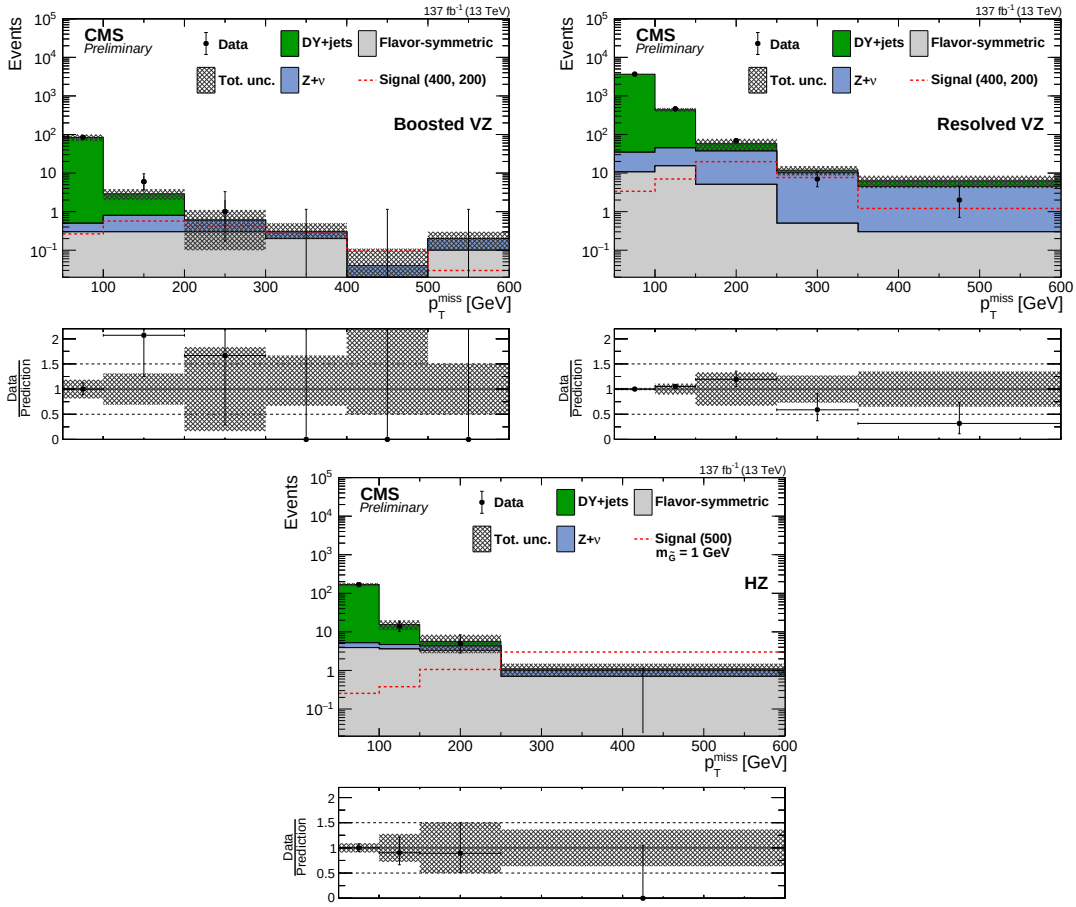

Figure 6: The $p_{\mathrm{T}}^{\mathrm{miss}}$ distribution in data is compared to the SM background prediction in the EW on-Z (upper left) boosted VZ, (upper right) resolved VZ, and (lower) HZ search regions, before the fits to data described in Section 8. The lower panel of each figure shows the ratio of observed data to the SM prediction in each $p_{\mathrm{T}}^{\mathrm{miss}}$ bin. The hashed band shows the total uncertainty in the background prediction, including statistical and systematic sources. The signal $p_{\mathrm{T}}^{\mathrm{miss}}$ distribution for the boosted and resolved VZ search regions correspond to the $\widetilde{\chi}_1^{\pm}$ $\widetilde{\chi}_2^0$ production model with a $\widetilde{\chi}_1^{\pm}/\widetilde{\chi}_2^0$ mass of 400 GeV and $\widetilde{\chi}_1^0$ mass of 200 GeV, while for the HZ search region the $p_{\mathrm{T}}^{\mathrm{miss}}$ distribution corresponds to a $\widetilde{\chi}_1^0$ pair production model decaying into a Higgs boson, a Z boson and two $\widetilde{\mathrm{G}}$, with the $\widetilde{\chi}_1^0$ and the $\widetilde{\mathrm{G}}$ having a mass of 500 GeV and 1 GeV. The $p_{\mathrm{T}}^{\mathrm{miss}}$ template prediction in each search region is normalized to the first $p_{\mathrm{T}}^{\mathrm{miss}}$ bin of each distribution in data.

from the limited size of the simulated samples. Finally, the further potential mismodeling of the lepton efficiencies and the $p_{\mathrm{T}}^{\mathrm{miss}}$ distributions associated with the CMS fast simulation framework are accounted for with an additional uncertainty. The assumed correlations in the signal uncertainties across SR are the same as those described in Section 5 for background processes.

8.2 Interpretations of the results using simplified SUSY models

The results in the strong on-Z search regions are interpreted using a SMS of gluino pair production, described in Section 1. This signal is characterized by final states with large hadronic activity. All strong on-Z SRs are included in the maximum likelihood fit, in order to maximize the acceptance to compressed scenarios where less hadronic activity is expected. Upper limits

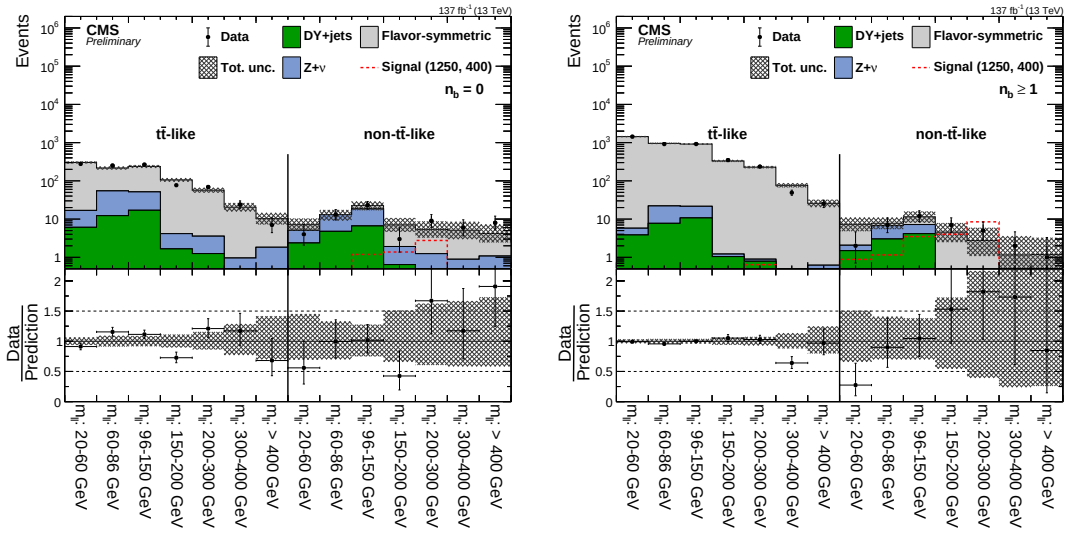

Figure 7: Results of the counting experiment in the edge search regions, before the fits to data described in Section 8. In each search region, the number of observed events in data (black markers) is compared to the SM background prediction, for the (left) b veto and (right) b tag categories. The hashed band shows the total uncertainty in the background prediction, including statistical and systematic sources.The signal distribution corresponds to the $\widetilde{b}$ pair production model, with the $\widetilde{b}$ having a mass of 1250 GeV and the $\widetilde{\chi}_2^0$ a mass of 400 GeV.

Table 8: Results of the $m_{\ell\ell}$ unbinned maximum likelihood fit to data in the edge fit search region, as defined in Table 2. The fitted yields of the Z + X and flavor-symmetric background components are tabulated, together with the fitted value of $R_{\mathrm{SF/DF}}$. The fitted signal contribution and the corresponding edge position are also shown. The local and global signal significances are expressed in terms of standard deviations (s.d.). The uncertainties include both statistical and systematic sources.

Z + X yield	447 ± 28
FS yield	1019 ± 29
$R_{\mathrm{SF/DF}}$	1.02 ± 0.04
Signal events	27 ± 22
$m_{\ell\ell}^{\mathrm{edge}}$	$293.4^{+12.6}_{-0.0}$ GeV
Local significance	1.3 s.d.
Global significance	0.7 s.d.

at 95% CL on the signal production cross section are shown in Fig. 10, as a function of the $\widetilde{g}$ and $\widetilde{\chi}_1^0$ masses, together with the expected and observed exclusion contours. We probe gluino masses up to 1600–1875 GeV, depending on the mass of $\widetilde{\chi}_1^0$, extending the reach of the previous CMS results [13] by about 100 GeV.

Upper limits at 95% CL on the production cross section of models of neutralino $\widetilde{\chi}_1^0$ pair production and chargino-neutralino ($\widetilde{\chi}_1^\pm\ \widetilde{\chi}_2^0$) production models are set using the results of the EW on-Z search regions.

For the model of $\widetilde{\chi}_1^\pm\ \widetilde{\chi}_2^0$ production with decays to $\mathrm{W}^\pm\mathrm{Z}$, the VZ search regions provide most of the sensitivity. While the resolved VZ search region is sensitive to a wide range of $\widetilde{\chi}_1^\pm/\widetilde{\chi}_2^0$ and $\widetilde{\chi}_1^0$ mass hypotheses, the boosted VZ region allows to improve the sensitivity for scenarios where the mass of the $\widetilde{\chi}_1^\pm/\widetilde{\chi}_2^0$ is much larger than the mass of $\widetilde{\chi}_1^0$, and the bosons produced in

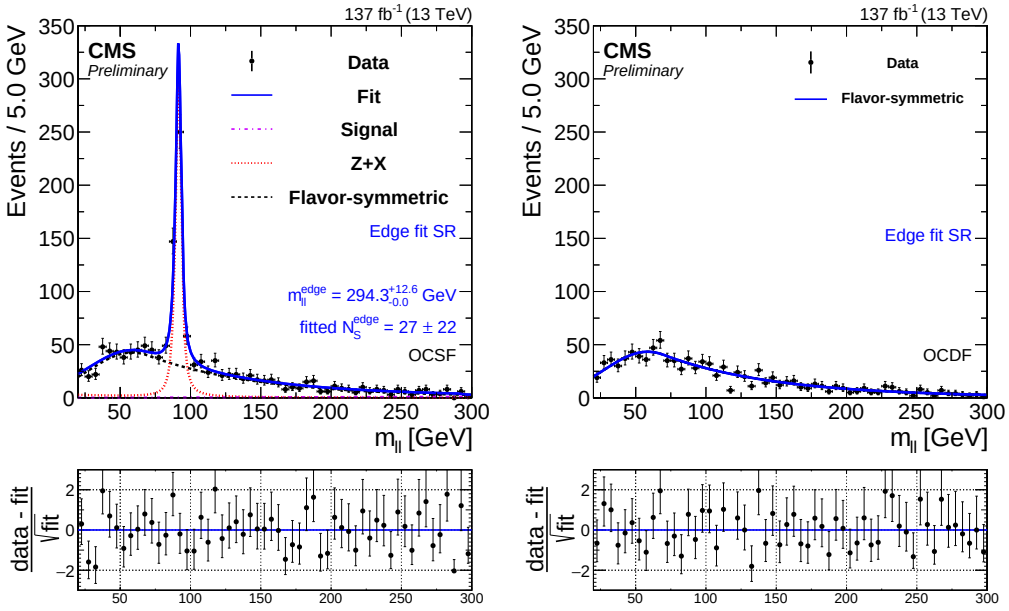

Figure 8: Fit to data of the dilepton mass ($m_{\ell\ell}$) distributions in the edge fit search regions, under the signal+background hypothesis, projected onto the (left) SF and (right) DF data samples. The fit shape is shown as a solid blue line. The individual fit components are indicated by dashed and dotted lines. The flavor-symmetric background is shown as a black dashed line. The Z + X background is displayed as a red dotted line. The extracted signal component is displayed as a purple dash-dotted line. The lower panel in each plot shows the difference between the observed data yield and the fit, divided by the square root of the number of fitted events.

the decay chain receive a large Lorentz boost. Figure 11 shows the cross section upper limits and the exclusion contours at 95% CL obtained for this model, as a function of the $\widetilde{\chi}_1^{\pm}/\widetilde{\chi}_2^0$ and $\widetilde{\chi}_1^0$ masses. We exclude $\widetilde{\chi}_1^{\pm}/\widetilde{\chi}_2^0$ masses up to 750 GeV, extending the reach of Ref. [13] by about 100 GeV. The observed exclusion limit is more stringent than the expected one, because of an underfluctuation of the observed data yields in the two highest $p_{\mathrm{T}}^{\mathrm{miss}}$ SRs of the resolved VZ search region (see Section 7.1).

Two scenarios are considered for the model of $\widetilde{\chi}_1^0$ pair production. One assumes that both $\widetilde{\chi}_1^0$ decay into a Z boson with 100% branching fraction. The other assumes that each $\widetilde{\chi}_1^0$ can decay to either a Z or a H boson with equal probability. The first scenario yields to final states with a pair of Z bosons, thus most of the signal events are expected to populate the VZ search regions. On the other hand, signal events where a H boson decays to $\mathrm{b\bar{b}}$ are expected to populate the HZ region. The observed and expected upper limits at 95% CL on the production cross section for both the considered scenarios are shown in Fig. 12. We are able to probe $\widetilde{\chi}_1^0$ masses up to 800 and 650 GeV, respectively, extending the reach of Ref. [13] by about 150 GeV.

The edge search regions are used to constrain the two slepton edge models presented in Section 1 (Fig. 2 (a) and (b)). Figure 13 shows the upper limits at 95% CL on the production cross section for both these models. We probe bottom (light-flavor) squark masses up to 1300–1600 (1600–1800) GeV, depending on the assumed $\widetilde{\chi}_2^0$ mass. For the case of bottom squark pair production, we improve the results from Ref. [13] by up to 300 GeV. The observed exclusion limits are more stringent than the expected ones for scenarios with low $\widetilde{\chi}_2^0$ mass. This is caused by a discrepancy between observed data yields and SM background predictions in the non-$\mathrm{t\bar{t}}$-like edge regions with $20 < m_{\ell\ell} < 60$ GeV (see Section 7.2).

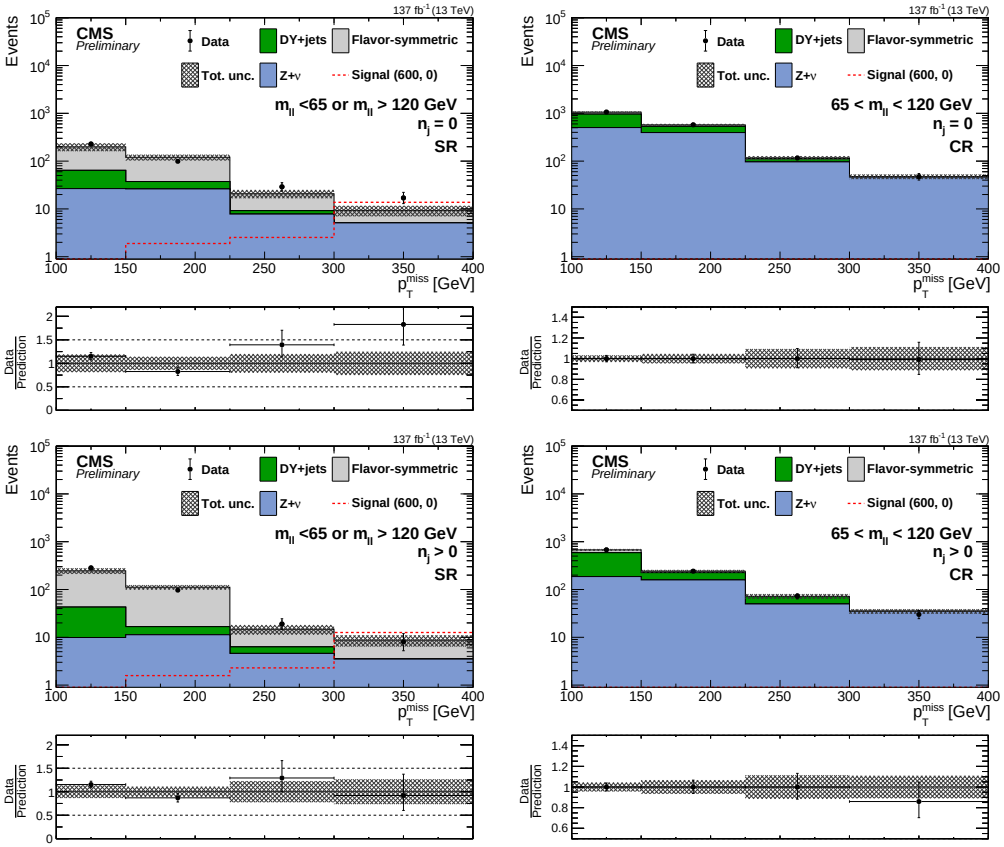

Figure 9: Distribution of $p_{\mathrm{T}}^{\mathrm{miss}}$ for events in the slepton (left) search regions and (right) control regions obtained by inverting the $m_{\ell\ell}$ selection, used to obtain the DY background normalization, for regions (upper) without jets and (lower) with jets. A background-only fit to data in the control region has been performed to determine the DY+jets contribution as described in section 8. The lower panel of each figure shows the ratio of observed data to the SM prediction in each $p_{\mathrm{T}}^{\mathrm{miss}}$ bin. The hashed band shows the total uncertainty in the background prediction, including statistical and systematic sources. The signal $p_{\mathrm{T}}^{\mathrm{miss}}$ distribution corresponds to the direct slepton pair production model, with a slepton mass of 600 GeV and a massless $\widetilde{\chi}_1^0$ particle.

Table 9: Predicted and observed event yields in the slepton search regions and control regions. A background-only fit to data in the control region has been performed to determine the DY+jets contribution as described in section 8. Uncertainties include both statistical and systematic sources.

$p_{\mathrm{T}}^{\mathrm{miss}}$ [GeV]	100–150	150–225	225–300	> 300
CR $65 < m_{\ell\ell} < 120\,\mathrm{GeV}$, $n_{\mathrm{j}} > 0$				
Flavor-symmetric	85 ± 11	15.7 ± 4.0	1.1 ± 0.9	$0.0^{+1.8}_{-0.0}$
DY+jets	402 ± 38	67 ± 21	21.1 ± 9.6	< 0.1
Z+ν	187 ± 20	159 ± 18	49.8 ± 6.1	34.9 ± 4.6
Total background	674 ± 29	241 ± 16	72.0 ± 8.2	34.9 ± 3.8
Data	674	241	72	30
CR $65 < m_{\ell\ell} < 120\,\mathrm{GeV}$, $n_{\mathrm{j}} = 0$				
Flavor-symmetric	98 ± 11	40.0 ± 6.8	2.0 ± 1.4	1.0 ± 0.8
DY+jets	458 ± 58	137 ± 46	18 ± 13	$0.0^{+0.8}_{-0.0}$
Z+ν	503 ± 53	396 ± 46	96 ± 12	46.4 ± 6.0
Total background	1059 ± 34	573 ± 26	116 ± 11	47.5 ± 5.3
Data	1059	573	116	47
SR $m_{\ell\ell} < 65$ or $m_{\ell\ell} > 120\,\mathrm{GeV}$, $n_{\mathrm{j}} > 0$				
Flavor-symmetric	203 ± 16	95 ± 11	8.4 ± 2.9	5.2 ± 2.3
DY+jets	33 ± 28	5.4 ± 5.6	1.7 ± 1.8	< 0.1
Z+ν	9.9 ± 1.4	11.3 ± 1.6	4.6 ± 0.6	3.5 ± 0.5
Total background	245 ± 33	112 ± 12	14.7 ± 3.3	8.7 ± 2.3
Data	283	97	19	8
SR $m_{\ell\ell} < 65$ or $m_{\ell\ell} > 120\,\mathrm{GeV}$, $n_{\mathrm{j}} = 0$				
Flavor-symmetric	134 ± 12	82.5 ± 9.5	11.6 ± 3.3	4.2 ± 2.2
DY+jets	38 ± 34	11 ± 13	1.4 ± 2.3	$0.0^{+0.1}_{-0.0}$
Z+ν	26.6 ± 3.7	26.2 ± 3.7	7.8 ± 1.1	5.1 ± 0.7
Total background	198 ± 37	120 ± 16	20.8 ± 4.1	9.3 ± 2.3
Data	228	99	29	17

The results in the slepton search regions are interpreted in the context of a slepton pair production model, introduced in Section 1. Upper limits at 95% CL on the signal production cross section are shown in Fig. 14. The observed exclusion is less stringent than the expected one, because of a discrepancy between observed data yields and SM background predictions in one $p_{\mathrm{T}}^{\mathrm{miss}}$ bin of the slepton region without jets (see Section 7.3). Slepton masses up to 650 GeV are probed for low $\tilde{\chi}_1^0$ masses, improving the previous CMS results [14] by about 200 GeV.

9 Summary

A search is presented for phenomena beyond the standard model in events with two opposite-charge, same-flavor leptons, and missing transverse momentum in the final state. The mea-

Table 10: Summary of the systematic uncertainties in the signal yields, together with their typical sizes across the search regions and the SMSs under consideration.

Source of uncertainty	Uncertainty (%)
Integrated luminosity	2.3–2.5
Limited size of simulated samples	1–15
Trigger efficiency	3
Lepton efficiency	5
Fast simulation lepton efficiency	4
b tag efficiency	0–5
Jet energy scale	0–5
Pileup modeling	1–2
ISR modeling	0–2.5
μ_R and μ_F variation	1–3
Fast simulation p_T^{miss} modeling	0–4

surements are performed in a sample of pp collisions at $\sqrt{s} = 13\,\text{TeV}$, collected with the CMS detector in 2016–2018, and corresponding to an integrated luminosity of $137\,\text{fb}^{-1}$. Search regions are defined in order to be sensitive to a wide range of new physics signatures. The observed data yields are found to be consistent with the SM background predictions, and the results are used to set upper limits on the production cross section of simplified models of supersymmetry. We probe gluino masses up to 1875 GeV, light-flavor (bottom) squark masses up

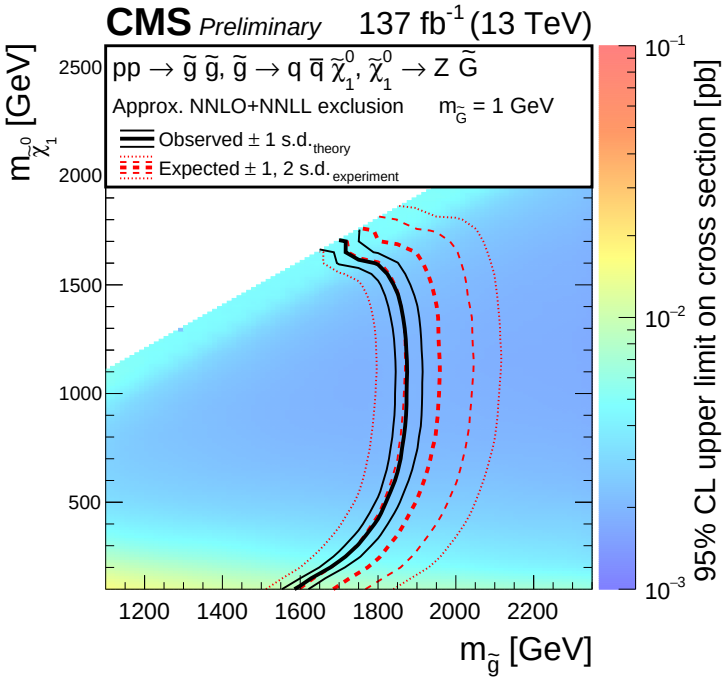

Figure 10: Cross section upper limits and exclusion contours at 95% CL for a SMS of GMSB gluino pair production, as a function of the $\tilde{g}$ and $\tilde{\chi}_1^0$ masses, obtained from the results in the strong on-Z search regions. The area enclosed by the thick black curve represents the observed exclusion region, while the dashed red lines indicate the expected limits and their ± 1 and ± 2 standard deviation (s.d.) ranges. The thin black lines show the effect of the theoretical uncertainties in the signal cross section.

to 1800 (1600) GeV, chargino (neutralino) masses up to 750 (800) GeV, and slepton masses up to 650 GeV, typically extending the reach of previous CMS results by hundreds of GeV.

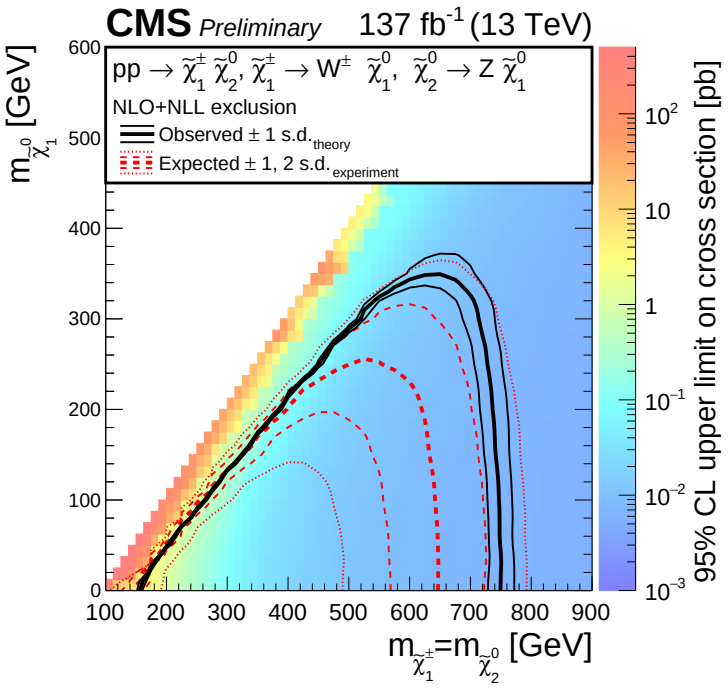

Figure 11: Cross section upper limits and exclusion contours at 95% CL for a SMS of $\widetilde{\chi}_1^{\pm}\ \widetilde{\chi}_2^0$ production, with final states containing a $W^{\pm}$ and a Z boson, as a function of the $\widetilde{\chi}_1^{\pm}/\widetilde{\chi}_2^0$ and $\widetilde{\chi}_1^0$ masses, obtained from the results in the EW on-Z search regions. The area enclosed by the thick black curve represents the observed exclusion region, while the dashed red lines indicate the expected limits and their ± 1 and ± 2 standard deviation (s.d.) ranges. The thin black lines show the effect of the theoretical uncertainties in the signal cross section.

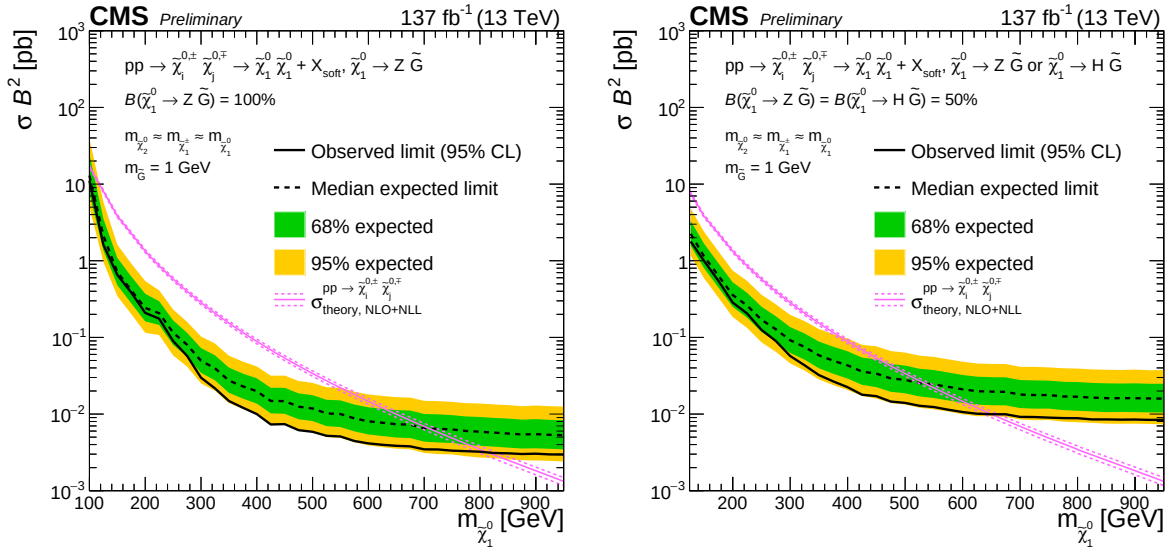

Figure 12: Production cross section upper limits at 95% CL as a function of the $\tilde{\chi}_1^0$ mass, for a model of EW $\tilde{\chi}_1^0$ pair production, where either (left) both $\tilde{\chi}_1^0$ decay into a Z boson with 100% branching fraction ($\mathcal{B}$), or (right) each $\tilde{\chi}_1^0$ can decay to a Z or a H boson with equal probability. The magenta curve shows the theoretical production cross section with its uncertainty. The solid (dashed) black line represents the observed (median expected) exclusion. The inner green (outer yellow) band indicates the region containing 68 (95)% of the distribution of limits expected under the background-only hypothesis.

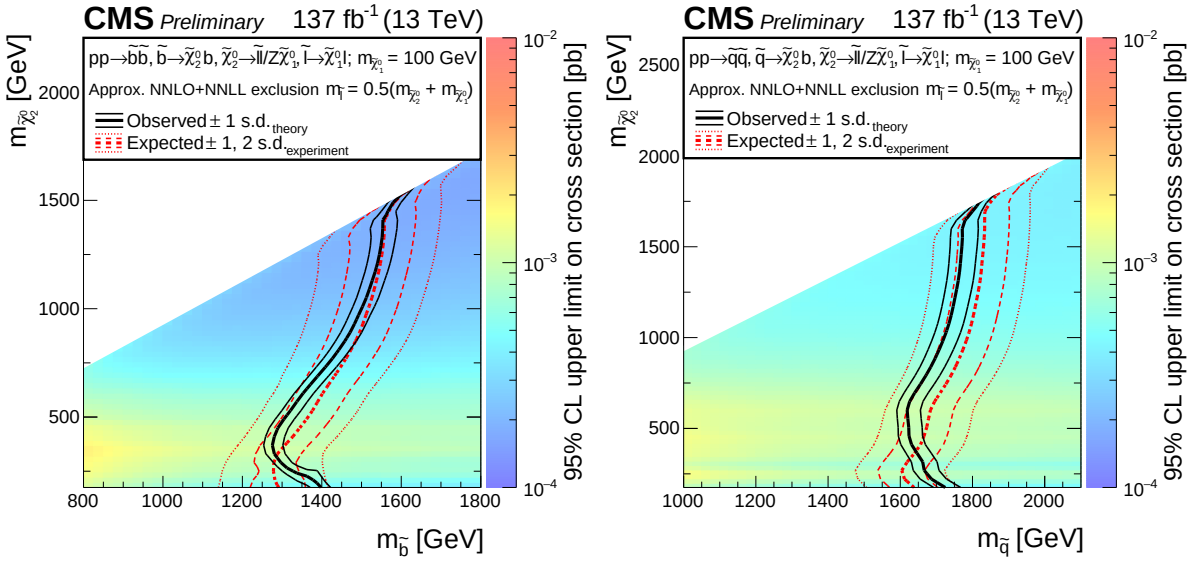

Figure 13: Cross section upper limits and exclusion contours at 95% CL for SMSs of (left) bottom and (right) light-flavor squark pair production, where each squark decays into a quark and a $\tilde{\chi}_2^0$, and the $\tilde{\chi}_2^0$ then decays via an intermediate slepton, forming a kinematic edge in the $m_{\ell\ell}$ distribution. The limits are obtained from the results in the edge search regions, and are shown as a function of the (left) $\tilde{b}$ or (right) $\tilde{q}$ and $\tilde{\chi}_2^0$ masses. The area enclosed by the thick black curve represents the observed exclusion region, while the dashed red lines indicate the expected limits and their ±1 and ±2 standard deviation (s.d.) ranges. The thin black lines show the effect of the theoretical uncertainties in the signal cross section.

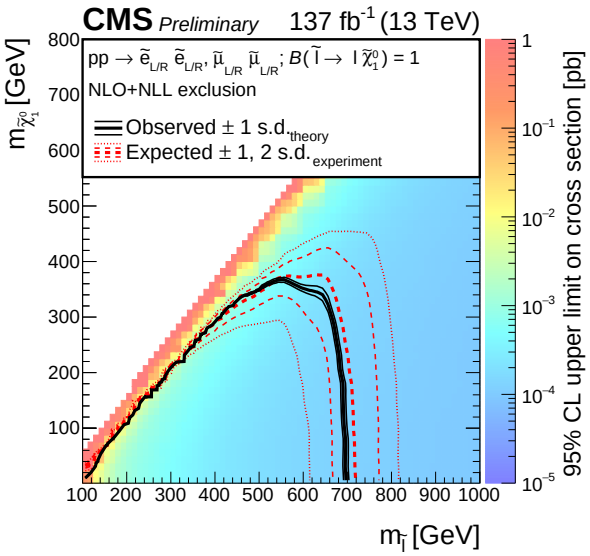

Figure 14: Cross section upper limits and exclusion contours at 95% CL for a SMS of slepton pair production, as a function of the slepton and $\widetilde{\chi}_1^0$ masses, obtained from the results in the slepton search regions. The area enclosed by the thick black curve represents the observed exclusion region, while the dashed red lines indicate the expected limits and their ± 1 and ± 2 standard deviation (s.d.) ranges. The thin black lines show the effect of the theoretical uncertainties in the signal cross section.

References

[1] G. Bertone, D. Hooper, and J. Silk, "Particle dark matter: Evidence, candidates and constraints", *Phys. Rept.* **405** (2005) 279–390, doi:10.1016/j.physrep.2004.08.031, arXiv:hep-ph/0404175.

[2] P. Ramond, "Dual theory for free fermions", *Phys. Rev. D* **3** (1971) 2415, doi:10.1103/PhysRevD.3.2415.

[3] Yu. A. Gol'fand and E. P. Likhtman, "Extension of the algebra of Poincaré group generators and violation of P invariance", *JETP Lett.* **13** (1971) 323.

[4] A. Neveu and J. H. Schwarz, "Factorizable dual model of pions", *Nucl. Phys. B* **31** (1971) 86, doi:10.1016/0550-3213(71)90448-2.

[5] D. V. Volkov and V. P. Akulov, "Possible universal neutrino interaction", *JETP Lett.* **16** (1972) 438.

[6] J. Wess and B. Zumino, "A Lagrangian model invariant under supergauge transformations", *Phys. Lett. B* **49** (1974) 52, doi:10.1016/0370-2693(74)90578-4.

[7] J. Wess and B. Zumino, "Supergauge transformations in four dimensions", *Nucl. Phys. B* **70** (1974) 39, doi:10.1016/0550-3213(74)90355-1.

[8] P. Fayet, "Supergauge invariant extension of the Higgs mechanism and a model for the electron and its neutrino", *Nucl. Phys. B* **90** (1975) 104, doi:10.1016/0550-3213(75)90636-7.

[9] H. P. Nilles, "Supersymmetry, supergravity and particle physics", *Phys. Rep.* **110** (1984) 1, doi:10.1016/0370-1573(84)90008-5.

[10] H. E. Haber and G. L. Kane, "The search for supersymmetry: Probing physics beyond the standard model", *Phys. Rept.* **117** (1985) 75, doi:10.1016/0370-1573(85)90051-1.

[11] G. R. Farrar and P. Fayet, "Phenomenology of the production, decay, and detection of new hadronic states associated with supersymmetry", *Phys. Lett. B* **76** (1978) 575, doi:10.1016/0370-2693(78)90858-4.

[12] J. Alwall, P. Schuster, and N. Toro, "Simplified Models for a First Characterization of New Physics at the LHC", *Phys. Rev. D* **79** (2009) 075020, doi:10.1103/PhysRevD.79.075020, arXiv:0810.3921.

[13] CMS Collaboration, "Search for new phenomena in final states with two opposite-charge, same-flavor leptons, jets, and missing transverse momentum in pp collisions at $\sqrt{s} = 13$ TeV", *JHEP* **03** (2018) 076, doi:10.1007/s13130-018-7845-2, 10.1007/JHEP03(2018)076, arXiv:1709.08908.

[14] CMS Collaboration, "Search for supersymmetric partners of electrons and muons in proton-proton collisions at $\sqrt{s} = 13$ TeV", *Phys. Lett. B* **790** (2019) 140, doi:10.1016/j.physletb.2019.01.005, arXiv:1806.05264.

[15] CMS Collaboration, "Search for physics beyond the Standard Model in events with two leptons, jets, and missing transverse momentum in pp collisions at $\sqrt{s} = 8$ TeV", *JHEP* **04** (2015) 124, doi:10.1007/JHEP04(2015)124, arXiv:1502.06031.

[16] CMS Collaboration, "Search for new physics in final states with two opposite-sign, same-flavor leptons, jets, and missing transverse momentum in pp collisions at $\sqrt{s} = 13$ TeV", *JHEP* **12** (2016) 013, doi:10.1007/JHEP12(2016)013, arXiv:1607.00915.

[17] CMS Collaboration, "Search for new physics in events with opposite-sign leptons, jets, and missing transverse energy in pp collisions at $\sqrt{s} = 7$ TeV", *Phys. Lett. B* **718** (2013) 815, doi:10.1016/j.physletb.2012.11.036, arXiv:1206.3949.

[18] CMS Collaboration, "Search for physics beyond the Standard Model in opposite-sign dilepton events in pp collisions at $\sqrt{s} = 7$ TeV", *JHEP* **06** (2011) 26, doi:10.1007/JHEP06(2011)026, arXiv:1103.1348.

[19] CMS Collaboration, "Searches for electroweak production of charginos, neutralinos, and sleptons decaying to leptons and W, Z, and Higgs bosons in pp collisions at 8 TeV", *Eur. Phys. J. C* **74** (2014) 3036, doi:10.1140/epjc/s10052-014-3036-7, arXiv:1405.7570.

[20] CMS Collaboration, "Searches for electroweak neutralino and chargino production in channels with Higgs, Z, and W bosons in pp collisions at 8 TeV", *Phys. Rev. D* **90** (2014) 092007, doi:10.1103/PhysRevD.90.092007, arXiv:1409.3168.

[21] ATLAS Collaboration, "Search for electroweak production of charginos and sleptons decaying into final states with two leptons and missing transverse momentum in $\sqrt{s} = 13$ TeV pp collisions using the ATLAS detector", *Eur. Phys. J. C* **80** (2020) 123, doi:10.1140/epjc/s10052-019-7594-6, arXiv:1908.08215.

[22] ATLAS Collaboration, "Search for supersymmetry in events containing a same-flavour opposite-sign dilepton pair, jets, and large missing transverse momentum in $\sqrt{s} = 8$ TeV pp collisions with the ATLAS detector", *Eur. Phys. J. C* **75** (2015) 318, doi:10.1140/epjc/s10052-015-3661-9, arXiv:1503.03290. [Erratum: *Eur. Phys. J. C* **75** (2015) 463].

[23] ATLAS Collaboration, "Search for the electroweak production of supersymmetric particles in $\sqrt{s} = 8$ TeV pp collisions with the ATLAS detector", *Phys. Rev. D* **93** (2016) 052002, doi:10.1103/PhysRevD.93.052002, arXiv:1509.07152.

[24] ATLAS Collaboration, "Search for new phenomena in events containing a same-flavour opposite-sign dilepton pair, jets, and large missing transverse momentum in $\sqrt{s} = 13$ TeV pp collisions with the ATLAS detector", *Eur. Phys. J. C* **77** (2017) 144, doi:10.1140/epjc/s10052-017-4700-5, arXiv:1611.05791.

[25] CMS Collaboration, "The CMS experiment at the CERN LHC", *JINST* **3** (2008) S08004, doi:10.1088/1748-0221/3/08/S08004.

[26] CMS Collaboration, "The CMS trigger system", *JINST* **12** (2017) P01020, doi:10.1088/1748-0221/12/01/P01020, arXiv:1609.02366.

[27] CMS Collaboration, "CMS technical design report for the pixel detector upgrade", Technical Report CERN-LHCC-2012-016, CMS-TDR-011, 2012. doi:10.2172/1151650.

[28] CMS Collaboration, "Particle-flow reconstruction and global event description with the CMS detector", *JINST* **12** (2017) P10003, doi:10.1088/1748-0221/12/10/P10003, arXiv:1706.04965.

[29] M. Cacciari, G. P. Salam, and G. Soyez, "The anti-k_t jet clustering algorithm", *JHEP* **04** (2008) 063, doi:10.1088/1126-6708/2008/04/063, arXiv:0802.1189.

[30] M. Cacciari, G. P. Salam, and G. Soyez, "FastJet user manual", *Eur. Phys. J. C* **72** (2012) 1896, doi:10.1140/epjc/s10052-012-1896-2, arXiv:1111.6097.

[31] CMS Collaboration, "Performance of the CMS muon detector and muon reconstruction with proton-proton collisions at $\sqrt{s} = 13$ TeV", *JINST* **13** (2018) P06015, doi:10.1088/1748-0221/13/06/P06015, arXiv:1804.04528.

[32] CMS Collaboration, "Performance of electron reconstruction and selection with the CMS detector in proton-proton collisions at $\sqrt{s} = 8$ TeV", *JINST* **10** (2015) P06005, doi:10.1088/1748-0221/10/06/P06005, arXiv:1502.02701.

[33] CMS Collaboration, "Performance of photon reconstruction and identification with the CMS detector in proton-proton collisions at $\sqrt{s} = 8$ TeV", *JINST* **10** (2015) P08010, doi:10.1088/1748-0221/10/08/P08010, arXiv:1502.02702.

[34] M. Cacciari and G. P. Salam, "Dispelling the N^3 myth for the k_t jet-finder", *Phys. Lett. B* **641** (2006) 57, doi:10.1016/j.physletb.2006.08.037, arXiv:hep-ph/0512210.

[35] CMS Collaboration, "Determination of jet energy calibration and transverse momentum resolution in CMS", *JINST* **6** (2011) P11002, doi:10.1088/1748-0221/6/11/P11002, arXiv:1107.4277.

[36] M. Cacciari and G. P. Salam, "Pileup subtraction using jet areas", *Phys. Lett. B* **659** (2008) 119, doi:10.1016/j.physletb.2007.09.077, arXiv:0707.1378.

[37] CMS Collaboration, "Identification of heavy-flavour jets with the CMS detector in pp collisions at 13 TeV", *JINST* **13** (2018) P05011, doi:10.1088/1748-0221/13/05/P05011, arXiv:1712.07158.

[38] A. J. Larkoski, S. Marzani, G. Soyez, and J. Thaler, "Soft Drop", *JHEP* **05** (2014) 146, doi:10.1007/JHEP05(2014)146, arXiv:1402.2657.

[39] J. Thaler and K. Van Tilburg, "Identifying Boosted Objects with N-subjettiness", *JHEP* **03** (2011) 015, doi:10.1007/JHEP03(2011)015, arXiv:1011.2268.

[40] CMS Collaboration, "Identification of heavy, energetic, hadronically decaying particles using machine-learning techniques", *JINST* **15** (2020) P06005, doi:10.1088/1748-0221/15/06/P06005, arXiv:2004.08262.

[41] J. Alwall et al., "The automated computation of tree-level and next-to-leading order differential cross sections, and their matching to parton shower simulations", *JHEP* **07** (2014) 079, doi:10.1007/JHEP07(2014)079, arXiv:1405.0301.

[42] P. Nason, "A new method for combining NLO QCD with shower Monte Carlo algorithms", *JHEP* **11** (2004) 040, doi:10.1088/1126-6708/2004/11/040, arXiv:hep-ph/0409146.

[43] S. Frixione, P. Nason, and C. Oleari, "Matching NLO QCD computations with parton shower simulations: the POWHEG method", *JHEP* **11** (2007) 070, doi:10.1088/1126-6708/2007/11/070, arXiv:0709.2092.

[44] S. Alioli, P. Nason, C. Oleari, and E. Re, "NLO single-top production matched with shower in POWHEG: s- and t-channel contributions", *JHEP* **09** (2009) 111, doi:10.1088/1126-6708/2009/09/111, arXiv:0907.4076. [Erratum: doi:10.1007/JHEP02(2010)011].

[45] S. Gieseke, T. Kasprzik, and J. H. Kühn, "Vector-boson pair production and electroweak corrections in HERWIG++", *Eur. Phys. J. C* **74** (2014) 2988, doi:10.1140/epjc/s10052-014-2988-y, arXiv:1401.3964.

[46] J. Baglio, L. D. Ninh, and M. M. Weber, "Massive gauge boson pair production at the LHC: a next-to-leading order story", *Phys. Rev. D* **88** (2013) 113005, doi:10.1103/PhysRevD.94.099902, 10.1103/PhysRevD.88.113005, arXiv:1307.4331. [Erratum: Phys. Rev. D 94, 099902 (2016)].

[47] A. Bierweiler, T. Kasprzik, and J. H. Kühn, "Vector-boson pair production at the LHC to $\mathcal{O}(\alpha^3)$ accuracy", *JHEP* **12** (2013) 071, doi:10.1007/JHEP12(2013)071, arXiv:1305.5402.

[48] J. M. Campbell and R. Ellis, "An Update on vector boson pair production at hadron colliders", *Phys. Rev. D* **60** (1999) 113006, doi:10.1103/PhysRevD.60.113006, arXiv:hep-ph/9905386.

[49] J. M. Campbell, R. Ellis, and C. Williams, "Vector boson pair production at the LHC", *JHEP* **07** (2011) 018, doi:10.1007/JHEP07(2011)018, arXiv:1105.0020.

[50] J. M. Campbell, R. K. Ellis, and W. T. Giele, "A Multi-Threaded Version of MCFM", *Eur. Phys. J. C* **75** (2015) 246, doi:10.1140/epjc/s10052-015-3461-2, arXiv:1503.06182.

[51] F. Caola, K. Melnikov, R. Röntsch, and L. Tancredi, "QCD corrections to ZZ production in gluon fusion at the LHC", *Phys. Rev. D* **92** (2015) 094028, doi:10.1103/PhysRevD.92.094028, arXiv:1509.06734.

[52] T. Sjöstrand et al., "An Introduction to PYTHIA 8.2", *Comput. Phys. Commun.* **191** (2015) 159, doi:10.1016/j.cpc.2015.01.024, arXiv:1410.3012.

[53] J. Alwall et al., "Comparative study of various algorithms for the merging of parton showers and matrix elements in hadronic collisions", *Eur. Phys. J. C* **53** (2008) 473, doi:10.1140/epjc/s10052-007-0490-5, arXiv:0706.2569.

[54] R. Frederix and S. Frixione, "Merging meets matching in MC@NLO", *JHEP* **12** (2012) 061, doi:10.1007/JHEP12(2012)061, arXiv:1209.6215.

[55] CMS Collaboration, "Event generator tunes obtained from underlying event and multiparton scattering measurements", *Eur. Phys. J. C* **76** (2016) 155, doi:10.1140/epjc/s10052-016-3988-x, arXiv:1512.00815.

[56] CMS Collaboration, "Extraction and validation of a new set of CMS PYTHIA8 tunes from underlying-event measurements", *Eur. Phys. J. C* **80** (2020) 4, doi:10.1140/epjc/s10052-019-7499-4, arXiv:1903.12179.

[57] NNPDF Collaboration, "Parton distributions for the LHC Run II", *JHEP* **04** (2015) 040, doi:10.1007/JHEP04(2015)040, arXiv:1410.8849.

[58] NNPDF Collaboration, "Parton distributions from high-precision collider data", *Eur. Phys. J. C* **77** (2017) 663, doi:10.1140/epjc/s10052-017-5199-5, arXiv:1706.00428.

[59] GEANT4 Collaboration, "GEANT4—a simulation toolkit", *Nucl. Instrum. Meth. A* **506** (2003) 250, doi:10.1016/S0168-9002(03)01368-8.

[60] S. Abdullin et al., "The fast simulation of the CMS detector at LHC", *J. Phys. Conf. Ser.* **331** (2011) 032049, doi:10.1088/1742-6596/331/3/032049.

[61] A. Giammanco, "The fast simulation of the CMS experiment", *J. Phys. Conf. Ser.* **513** (2014) 022012, doi:10.1088/1742-6596/513/2/022012.

[62] E. Re, "Single-top Wt-channel production matched with parton showers using the POWHEG method", *Eur. Phys. J. C* **71** (2011) 1547, doi:10.1140/epjc/s10052-011-1547-z, arXiv:1009.2450.

[63] R. Gavin, Y. Li, F. Petriello, and S. Quackenbush, "FEWZ 2.0: A code for hadronic Z production at next-to-next-to-leading order", *Comput. Phys. Commun.* **182** (2011) 2388, doi:10.1016/j.cpc.2011.06.008, arXiv:1011.3540.

[64] R. Gavin, Y. Li, F. Petriello, and S. Quackenbush, "W physics at the LHC with FEWZ 2.1", *Comput. Phys. Commun.* **184** (2013) 208, doi:10.1016/j.cpc.2012.09.005, arXiv:1201.5896.

[65] M. Czakon and A. Mitov, "Top++: a program for the calculation of the top-pair cross-section at hadron colliders", *Comput. Phys. Commun.* **185** (2014) 2930, doi:10.1016/j.cpc.2014.06.021, arXiv:1112.5675.

[66] W. Beenakker et al., "The Production of charginos / neutralinos and sleptons at hadron colliders", *Phys. Rev. Lett.* **83** (1999) 3780, doi:10.1103/PhysRevLett.100.029901, arXiv:hep-ph/9906298. [Erratum: Phys.Rev.Lett. 100, 029901 (2008)].

[67] G. Bozzi, B. Fuks, and M. Klasen, "Threshold resummation for slepton-pair production at hadron colliders", *Nucl. Phys. B* **777** (2007) 157, doi:10.1016/j.nuclphysb.2007.03.052.

[68] J. Debove, B. Fuks, and M. Klasen, "Threshold resummation for gaugino pair production at hadron colliders", *Nucl. Phys. B* **842** (2011) 51, doi:10.1016/j.nuclphysb.2010.08.016, arXiv:1005.2909.

[69] B. Fuks, M. Klasen, D. R. Lamprea, and M. Rothering, "Gaugino production in proton-proton collisions at a center-of-mass energy of 8 TeV", *JHEP* **10** (2012) 081, doi:10.1007/JHEP10(2012)081, arXiv:1207.2159.

[70] B. Fuks, M. Klasen, D. R. Lamprea, and M. Rothering, "Precision predictions for electroweak superpartner production at hadron colliders with RESUMMINO", *Eur. Phys. J. C* **73** (2013) 2480, doi:10.1140/epjc/s10052-013-2480-0, arXiv:1304.0790.

[71] B. Fuks, M. Klasen, D. R. Lamprea, and M. Rothering, "Revisiting slepton pair production at the Large Hadron Collider", *JHEP* **01** (2014) 168, doi:10.1007/JHEP01(2014)168, arXiv:1310.2621.

[72] J. Fiaschi and M. Klasen, "Neutralino-chargino pair production at NLO+NLL with resummation-improved parton density functions for LHC Run II", *Phys. Rev. D* **98** (2018), no. 5, 055014, doi:10.1103/PhysRevD.98.055014, arXiv:1805.11322.

[73] J. Fiaschi and M. Klasen, "Slepton pair production at the LHC in NLO+NLL with resummation-improved parton densities", *JHEP* **03** (2018) 094, doi:10.1007/JHEP03(2018)094, arXiv:1801.10357.

[74] W. Beenakker, R. Höpker, M. Spira, and P. M. Zerwas, "Squark and gluino production at hadron colliders", *Nucl. Phys. B* **492** (1997) 51, doi:10.1016/S0550-3213(97)00084-9, arXiv:hep-ph/9610490.

[75] W. Beenakker et al., "Stop production at hadron colliders", *Nucl. Phys. B* **515** (1998) 3, doi:10.1016/S0550-3213(98)00014-5, arXiv:hep-ph/9710451.

[76] A. Kulesza and L. Motyka, "Threshold resummation for squark-antisquark and gluino-pair production at the LHC", *Phys. Rev. Lett.* **102** (2009) 111802, doi:10.1103/PhysRevLett.102.111802, arXiv:0807.2405.

[77] A. Kulesza and L. Motyka, "Soft gluon resummation for the production of gluino-gluino and squark-antisquark pairs at the LHC", *Phys. Rev. D* **80** (2009) 095004, doi:10.1103/PhysRevD.80.095004, arXiv:0905.4749.

[78] W. Beenakker et al., "Soft-gluon resummation for squark and gluino hadroproduction", *JHEP* **12** (2009) 041, doi:10.1088/1126-6708/2009/12/041, arXiv:0909.4418.

[79] W. Beenakker et al., "Supersymmetric top and bottom squark production at hadron colliders", *JHEP* **08** (2010) 098, doi:10.1007/JHEP08(2010)098, arXiv:1006.4771.

[80] W. Beenakker et al., "Squark and gluino hadroproduction", *Int. J. Mod. Phys. A* **26** (2011) 2637, doi:10.1142/S0217751X11053560, arXiv:1105.1110.

[81] W. Beenakker et al., "NNLL resummation for squark-antisquark pair production at the LHC", *JHEP* **01** (2012) 076, doi:10.1007/JHEP01(2012)076, arXiv:1110.2446.

[82] W. Beenakker et al., "Towards NNLL resummation: hard matching coefficients for squark and gluino hadroproduction", *JHEP* **10** (2013) 120, doi:10.1007/JHEP10(2013)120, arXiv:1304.6354.

[83] W. Beenakker et al., "NNLL resummation for squark and gluino production at the LHC", *JHEP* **12** (2014) 023, doi:10.1007/JHEP12(2014)023, arXiv:1404.3134.

[84] W. Beenakker et al., "NNLL resummation for stop pair-production at the LHC", *JHEP* **05** (2016) 153, doi:10.1007/JHEP05(2016)153, arXiv:1601.02954.

[85] W. Beenakker et al., "NNLL-fast: predictions for coloured supersymmetric particle production at the LHC with threshold and Coulomb resummation", *JHEP* **12** (2016) 133, doi:10.1007/JHEP12(2016)133, arXiv:1607.07741.

[86] C. G. Lester and D. J. Summers, "Measuring masses of semiinvisibly decaying particles pair produced at hadron colliders", *Phys. Lett. B* **463** (1999) 99, doi:10.1016/S0370-2693(99)00945-4, arXiv:hep-ph/9906349.

[87] A. Barr, C. Lester, and P. Stephens, "A variable for measuring masses at hadron colliders when missing energy is expected; M_{T2}: the truth behind the glamour", *J. Phys. G* **29** (2003) 2343, doi:10.1088/0954-3899/29/10/304, arXiv:hep-ph/0304226.

[88] Particle Data Group, C. Patrignani et al., "Review of Particle Physics", *Chin. Phys. C* **40** (2016) 100001, doi:10.1088/1674-1137/40/10/100001.

[89] E. Gross and O. Vitells, "Trial factors or the look elsewhere effect in high energy physics", *Eur. Phys. J. C* **70** (2010) 525, doi:10.1140/epjc/s10052-010-1470-8, arXiv:1005.1891.

[90] T. Junk, "Confidence level computation for combining searches with small statistics", *Nucl. Instrum. Meth. A* **434** (1999) 435, doi:10.1016/S0168-9002(99)00498-2, arXiv:hep-ex/9902006.

[91] A. L. Read, "Presentation of search results: the CL_s technique", *J. Phys. G* **28** (2002) 2693, doi:10.1088/0954-3899/28/10/313.

[92] G. Cowan, K. Cranmer, E. Gross, and O. Vitells, "Asymptotic formulae for likelihood-based tests of new physics", *Eur. Phys. J. C* **71** (2011) 1554, doi:10.1140/epjc/s10052-011-1554-0, arXiv:1007.1727. [Erratum: doi:10.1140/epjc/s10052-013-2501-z].

[93] ATLAS and CMS Collaborations, "Procedure for the LHC Higgs boson search combination in summer 2011", ATLAS/CMS joint note ATL-PHYS-PUB-2011-011, CMS-NOTE-2011-005, 2011.

[94] CMS Collaboration, "CMS luminosity measurements for the 2016 data-taking period", CMS Physics Analysis Summary CMS-PAS-LUM-17-001, 2017.

[95] CMS Collaboration, "CMS luminosity measurement for the 2017 data-taking period at $\sqrt{s} = 13\,\text{TeV}$", CMS Physics Analysis Summary CMS-PAS-LUM-17-004, 2018.

[96] CMS Collaboration, "CMS luminosity measurement for the 2018 data-taking period at $\sqrt{s} = 13\,\text{TeV}$", CMS Physics Analysis Summary CMS-PAS-LUM-18-002, 2019.